Journal of Zhejiang University-SCIENCE A (Applied Physics & Engineering)
ISSN 1673-565X (Print); ISSN 1862-1775 (Online)
www.zju.edu.cn/jzus; www.springerlink.com
E-mail: jzus@zju.edu.cn

Improving the wind and temperature measurements of an airborne meteorological measuring system

Stephen FOSTER[1], P. W. CHAN[†‡2]

([1]*Aventech Research Inc., Barrie, ON L4N 2E3, Canada*)

([2]*Hong Kong Observatory, Kowloon, Hong Kong, China*)

[†]E-mail: pwchan@hko.gov.hk

Received Sept. 19, 2011; Revision accepted Aug. 30, 2012; Crosschecked Aug. 30, 2012

Abstract: The Aircraft Integrated Meteorological Measuring System 20 Hz (AIMMS-20) has been used by the Hong Kong Observatory (HKO), China in data collection for tropical cyclone situations over the South China Sea and windshear and turbulence measurement at the Hong Kong International Airport (HKIA). This paper discusses possible methods for further enhancing the quality of the wind and temperature measurements from the system. For wind measurement, the enhancement methods include: error modelling of the accelerometer (e.g., bias offset and cross-axis rate sensitivity), global positioning system (GPS) phase lag consideration, better representation of the inertial measurement unit (IMU) velocity based on the GPS velocities and considering their location differences, consideration of the slower update of GPS velocity, and wing flexure. For temperature measurement, the methods include the consideration of the temperature sensor response and the sensor housing response. The results of typical flights using AIMMS-20 show that the accuracy of the wind and temperature data could be improved by 20%–30%. Though the discussion in the present paper is related mainly to a specific meteorological measuring system on a particular aircraft, the techniques so employed should be a useful reference for similar systems installed on other aircraft.

Key words: Airborne meteorological measurements, Kalman filter, Comparison with radiosonde measurement
doi:10.1631/jzus.A1100245 **Document code:** A **CLC number:** P43

1 Introduction

A windshear alerting service is provided by the Hong Kong Observatory (HKO) at the Hong Kong International Airport (HKIA). During verification of the service, pilot windshear reports are regularly obtained from aircraft through air traffic control. For more objective verification, aircraft data are also collected to study the windshear data. Such aircraft data include the quick access recorder (QAR) data collected by the airlines. Moreover, in the mid of 2009, a meteorological measuring system was first installed on an aircraft in Hong Kong to collect weather data necessary for windshear verification purposes. The system is the Aircraft Integrated Meteorological Measuring System 20 Hz (AIMMS-20). The aircraft is one of the Jetstream 4100 (J4100) fixed-wing aircraft of the Government Flying Service (GFS) of the Hong Kong Government, which is primarily used for search and rescue (SAR) operations over the South China Sea. When it is not required to perform SAR operations, the aircraft also helps collect wind and turbulence data routinely.

The AIMMS-20 system was calibrated in the factory as well as in a calibration flight. The technical specifications for wind and temperature data are shown in Table 1.

The system has been used for observing a tropical cyclone over the South China Sea (Chan *et al*., 2011) and measuring windshear and turbulence at the HKIA.

The use of instrumented aircraft in the collection of meteorological data dates back to the 1970s

‡ Corresponding author

© Zhejiang University and Springer-Verlag Berlin Heidelberg 2012

(Telford *et al*., 1977). A review of the technology can be found in (Lenschow, 1986). There have been reviews of the various instrumented aircraft used for meteorological data collection purpose, such as the Falcon of DLR (Bögel and Baumann, 1991) and Meteopod (Vörsmann, 1990). The quality of aircraft data has been studied by, for instance, Dobosy *et al*. (1997) and Drüe *et al*. (2008). Improvements to the meteorological measurements on the aircraft, including wind and temperature measurements, have also been described (Inverarity, 2000; Khelif *et al*., 1999; Matejka and Lewis, 1997; Rodi and Spyers-Duran, 1972).

Table 1 Specifications of the AIMMS-20 system

Parameter	Horizontal wind (m/s)	Temperature (°C)
Range	0–±90	−20–50
Accuracy	0.5 for straight level flight; 1 otherwise with bank angle less than 15°	0.3
Resolution	0.1	0.1

This paper considers the possibility of improving the accuracy of wind and temperature data measured by AIMMS-20 through use of a post-processing technique. Though the discussion relates mainly to a specific meteorological measuring system, namely the AIMMS-20 on the aircraft, the techniques considered should be a useful reference for similar systems installed on other aircraft.

2 A review of the AIMMS-20 system

The airborne wind-measurement problem requires the following pieces of information in order to obtain a solution:

1. A 3D air-flow vector measured in an aircraft-fixed reference frame;

2. Aircraft orientation relative to the inertial reference frame;

3. Aircraft velocity relative to the inertial reference frame.

The AIMMS-20 system measures the local flow vector, i.e., the aircraft-relative wind vector, using aerodynamically generated differential pressures about a hemispherical 5-hole probe tip combined with a separate static-pressure ring located a few inches downstream on the cylindrical probe body. Transforming these pressures into flow velocity and direction requires additional data, specifically temperature, humidity and barometric (static) pressure. The AIMMS air-data probe (ADP) integrates all pressure, temperature, and humidity sensors in a single probe assembly. Also, three accelerometers are embedded inside the probe to aid in tracking high-frequency motions in support of turbulence calculations. Included within the ADP are digitizing, processing and communication electronics so that the device appears to the rest of the system as an intelligent node on a digital network.

The ADP is a 1.5 kg probe mounted about 4″ below the lower-wing surface at the wing-tip. The probe is a 1.5″ diameter aluminum tube with a titanium nitride coating that projects 18″ forward of the main support body. Anti-ice heaters (150 W@28 V) are embedded within the probe tip to prevent pressure port blockage under icing conditions. Temperature and humidity are measured within an aft semi-elliptical housing, which generates flow inside a ventilation tube via suction holes. The flow is drawn backwards through the tube from the rear stagnation zone at the end of the probe. A single multi-conductor network cable is run inside the wing to deliver both power and network communications. The ADP appears to the rest of the system as a data-generating network node that places fully compensated/calibrated air-data parameters on a controller-area-network (CAN) serial bus at 500 kbps.

The second and third parts of the measurement problem involve determining the attitude and velocity of the aircraft in inertial space. The AIMMS-20 employs a novel global positioning system (GPS)-inertial integration strategy combining data from a GPS module with data from an inertial measurement unit module (IMU). The IMU supplies rate measurements from a triad of accelerometers and gyros. Data from each module is placed on the CAN bus and a third module, and the central processing module (CPM) reads this information and applies digital filter algorithms to solve for attitude and inertial velocity. Further, the CPM firmware applies dynamic and aerodynamic corrections to air-data and combines this with attitude and inertial velocity to complete real-time meteorological data reduction.

Attitude is resolved by two different and complementary means. The first uses an accelerometer

triad from which body forces, due to the combined influence of gravity and inertia, are measured in an aircraft-fixed frame. The orientation of the aircraft frame is determined by reconciling measured acceleration vectors against that observed in the inertial frame by the GPS. Satellite signal Doppler shifts, which are directly proportional to velocity along the line-of-sight, are measured and utilized by the GPS processor. Velocity, therefore, is a primary measurement within the GPS system. Attitude can be resolved by reconciling GPS velocity output with once-integrated accelerometer data, or by reconciling time-differenced GPS velocity with direct accelerometer output. The former scheme was chosen as integration is inherently noise reducing in contrast to time-differencing, which acts to increase signal noise.

Range data derived from satellite signal time-of-flight are another primary measurement subset of the GPS navigation system. However, reconciling orientation of measured acceleration vectors with GPS position would entail double time-integration of accelerometer output. Although feasible, such a scheme would increase the mathematical complexity of the resulting Kalman filter with increased costs in terms of processing time per update cycle. Matching once-integrated IMU rates with GPS velocity was, therefore, selected as the preferred basis for developing the first Kalman filter. This filter estimates IMU rate-integration errors, which are then applied to correct IMU output. The integrated IMU outputs are refreshed at 40 Hz, but the Kalman filter that derives IMU attitude and velocity errors is run at 5 Hz using GPS velocity data provided at the same rate.

A second Kalman filter is dedicated to determining separate estimates for roll and heading angles from GPS satellite carrier-phase data acquired for all satellites in view from each of two wing-tip mounted antennas. This filter exploits inertial rates from the IMU to solve rapidly the initial phase-ambiguity problem (initial unknown constant of integration), which must be solved by any carrier-phase based attitude algorithm. Rapid solution convergence is further aided by having an excellent initial attitude guess from the first filter.

This GPS carrier-phase filter is necessary to provide a precise, stable true-heading reference. A stable heading reference is necessary during steady flight because under such conditions there is very little in the way of an acceleration signal in the horizontal plane, which is normally used to establish the heading orientation of the accelerometer triad. The IMU's angular rate sensors provide good coasting performance between acceleration inputs, but they will wander slowly with time without additional information to check gyro drift. With carrier-phase stability equivalent to a few mm and an antenna baseline of 18 m, the angular precision limit for this method is at the level of a few 0.01° and it is perfectly stable with a consistent set of satellite signals during level flight. This method, therefore, is well suited as a long-period stable heading reference, which is at least a full order of magnitude better than what can be obtained using geomagnetic field measurement methods.

In spite of the high levels of precision, the differential carrier phase solution is not employed exclusively because it can suffer from phase-tracking cycle slips. Such cycle slips frequently occur when an aircraft rolls into a banked turn, potentially wreaking havoc on a given set of satellite signals due to rapid changes in antenna orientation. However, IMU information can be used to manage this potential toward phase-filter instability. As it operates as an independent filter, the carrier-phase solution can be shut down completely and subsequently re-initialized with accurate attitude data from the IMU without causing any disturbances to the primary attitude solution. The phase solution can be brought in and out of the process as conditions merit: it is eliminated during episodes of high dynamics and brought in to fine-tune and stabilize IMU output in steady flight. As a result, these two Kalman filter processes are very much complementary.

The flow of information from primary sensor sources to the final wind solution is summarized in Fig. 1.

A final module was added to the AIMMS-20 system to perform automatic data recording for the GFS J4100 installation. This feature was important to minimize the amount of interaction between the flight crew and the AIMMS-20 to keep the operational overhead as low as possible. Following the rest of the system design, the digital I/O module (DIO) is a modular network node connected to the system CAN bus. Included with the DIO module is a USB thumb drive receptacle that supports a miniature format

FLASH drive, with a storage capacity of up to 8 GB. As it is connected to the CAN bus, the DIO module has full access to all information from all modules, plus it can read meteorological data broadcasts from the CPM performed in real time. DIO firmware monitors aircraft speed from the GPS data stream. The firmware opens log files once the speed exceeds 20 m/s, and closes log files once this speed decreases below 5 m/s. The filenames used are automatically generated using the date (month and day number) and the time, likewise obtained from GPS data. Two sets of files are created on each flight: one set records all raw system data, essentially a facsimile of all CAN-bus traffic, and the second set is an ASCII file in a tabular format, updated at 5 Hz, containing the processed data. The ASCII file set is provided for convenience and the raw data set is used to support PC-based post-processing. With this system, GFS staff need only periodically remove the thumb drive and transfer files using any standard PC/Windows compatible computer.

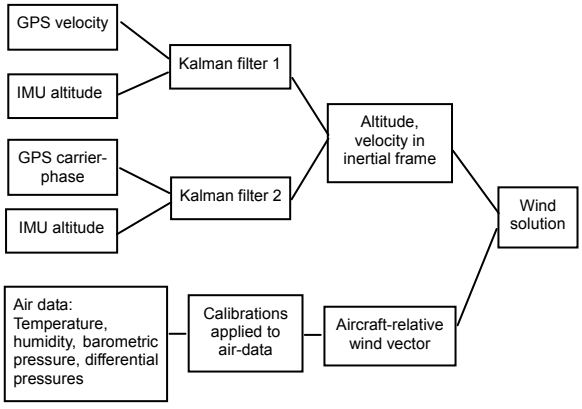

Fig. 1 Wind solution schematic

Areas for improvement in meteorological data quality can be grouped, therefore, into two general categories: (1) GPS-inertial data handling affecting attitude and velocity in the inertial frame; and, (2) air-data corrections affecting the aircraft-relative wind vector.

2.1 Overview of Kalman filter 1

The orientation of the IMU with respect to the earth-fixed frame is described by a set of three Euler angles: ϕ (roll), θ (pitch), and ψ (heading). These rotations are applied in the so-called 3-2-1 rotation order, i.e., the heading rotation is applied first about the vertical (z) axis, followed by a rotation about the intermediate pitch (y) axis and a third and final rotation about the final roll (x) axis (Etkin, 1982). Attitude at any given time is given by continuous integration of Euler angle rates:

$$\phi_n = \phi_0 + \int_{t_0}^{t_n} \dot{\phi}(t)\mathrm{d}t, \tag{1}$$

$$\theta_n = \theta_0 + \int_{t_0}^{t_n} \dot{\theta}(t)\mathrm{d}t, \tag{2}$$

$$\psi_n = \psi_0 + \int_{t_0}^{t_n} \dot{\psi}(t)\mathrm{d}t, \tag{3}$$

where the Euler rates are derived from three angular rates, P, Q and R, defined in the IMU-fixed reference frame, representing rotations about the IMU X, Y, and Z axes, respectively. The transformations of these "gyro" sensor rates to Euler rates are given by

$$\dot{\phi} = P + Q\sin\phi\tan\theta + R\cos\phi\tan\theta, \tag{4}$$

$$\dot{\theta} = Q\cos\phi - R\sin\phi, \tag{5}$$

$$\dot{\psi} = \frac{(Q\sin\phi + R\cos\phi)}{\cos\theta}. \tag{6}$$

Similarly, inertial velocity vector, $\boldsymbol{\vartheta}$, is continually updated by integration of acceleration $\boldsymbol{a}$ in the inertial frame:

$$\boldsymbol{\vartheta}_n = \boldsymbol{\vartheta}_0 + \int_{t_0}^{t_n} \boldsymbol{a}(t)\mathrm{d}t. \tag{7}$$

This acceleration vector is obtained from three-component measurements, $\boldsymbol{a}_\mathrm{b}$, made in the body-fixed IMU reference frame according to the following transformation:

$$\boldsymbol{a}=\boldsymbol{C}_\mathrm{eb}(\phi, \theta, \psi)\boldsymbol{a}_\mathrm{b}+g\boldsymbol{e}_3, \tag{8}$$

where $\boldsymbol{C}_\mathrm{eb}$ is a general 3×3 rotational transformation matrix that converts coordinates in the body-fixed IMU frame to the earth-fixed frame given the Euler angle triplet defining orientation of the body frame relative to the earth-fixed frame (Etkin, 1982), g is acceleration due to gravity and $\boldsymbol{e}_3$ is the unit vector aligned with the vertical coordinate direction of the earth frame (positive down).

A Kalman filter is applied to estimate errors that propagate through rate integrations of Eqs. (1)–(3) and Eq. (7) by optimal fitting of a system-error model that seeks to minimize the uncertainty between the predicted velocity $\hat{\boldsymbol{\vartheta}}$, derived from the IMU integrated velocity $\boldsymbol{\vartheta}_i$ and the estimated IMU error vector $\delta\boldsymbol{\vartheta}$, and the best estimate of the velocity of the IMU in inertial space derived from GPS velocity output $\boldsymbol{\vartheta}_{\mathrm{GPS}}$, i.e., to minimize the 2-norm of the following error vector:

$$\boldsymbol{\epsilon}=\boldsymbol{\vartheta}_{\mathrm{GPS}}-(\boldsymbol{\vartheta}_i-\delta\boldsymbol{\vartheta}). \tag{9}$$

An error model for the behaviour of $\delta\boldsymbol{\vartheta}$ is developed by first recognizing that the IMU integration process will include acceleration and angular rates that are not perfect and hence errors $\delta\boldsymbol{a}(t)$ will be integrated along with the true values resulting in the following propagation of velocity error:

$$\delta\boldsymbol{\vartheta}_{n+1}=\delta\boldsymbol{\vartheta}_n+\int_{t_n}^{t_{n+1}}\delta\boldsymbol{a}(t)\mathrm{d}t. \tag{10}$$

The acceleration error is, in turn, related to attitude error via Eq. (8) for a given set of IMU accelerometer sensor readings according to the following:

$$\delta\boldsymbol{a}=\boldsymbol{a}_{\mathrm{b}}\frac{\partial\boldsymbol{C}_{\mathrm{eb}}}{\partial\phi}\delta\phi+\boldsymbol{a}_{\mathrm{b}}\frac{\partial\boldsymbol{C}_{\mathrm{eb}}}{\partial\theta}\delta\theta+\boldsymbol{a}_{\mathrm{b}}\frac{\partial\boldsymbol{C}_{\mathrm{eb}}}{\partial\psi}\delta\psi. \tag{11}$$

Attitude-error is propagated through time according to the following first-order model:

$$\begin{aligned}\delta\phi_{n+1}&=\delta\phi_n+\delta\dot{\phi}_n\Delta t,\\ \delta\theta_{n+1}&=\delta\theta_n+\delta\dot{\theta}_n\Delta t,\\ \delta\psi_{n+1}&=\delta\psi_n+\delta\dot{\psi}_n\Delta t.\end{aligned} \tag{12}$$

Rate errors ($\delta\dot{\phi}$, $\delta\dot{\theta}$, $\delta\dot{\psi}$) are, in turn, estimated by taking first-order differentials of Eqs. (4), (5) and (6) with respect to gyro rates (P, Q, R) and Euler angles (ϕ, θ, ψ), respectively, resulting in a functional dependency of the form,

$$(\delta\dot{\phi},\delta\dot{\theta},\delta\dot{\psi})=H(\delta P,\delta Q,\delta R,\delta\phi,\delta\theta,\delta\psi). \tag{13}$$

Gyro rate errors are modelled according to a fixed rate zero-offset plus a first-order linear cross-axis sensitivity to angular rates about the other two perpendicular axes:

$$\begin{aligned}\delta P&=P_0+Q\delta\psi_1-R\delta\theta_1,\\ \delta Q&=Q_0+R\delta\phi_2-P\delta\psi_2,\\ \delta R&=R_0+P\delta\theta_3-Q\delta\phi_3,\end{aligned} \tag{14}$$

where the cross-axis error is represented as an angular offset of the rate sensor from the ideal axis, e.g., $\delta\psi_1$ is the perturbation in the yaw direction of the roll gyro such that it will resolve a component of the pitch rate Q onto the roll-gyro's sensing axis; and, similarly, $\delta\theta_1$ is the perturbation in the pitch direction of the roll gyro such that it will resolve a component of the yaw rate onto the roll-gyro's sensing axis.

Under normal operation, the Kalman filter takes a series of observations for $\delta\boldsymbol{\vartheta}$ using GPS velocity data and implicitly estimates the following parameters based on achieving a best-fit with the error-model scheme: attitude errors ($\delta\phi$, $\delta\theta$, $\delta\psi$); the parameters controlling their rates of change (P_0, Q_0, R_0); and, smoothed estimates for velocity component errors (δu, δv, δw). All of these errors estimates are with reference to the continuous IMU rate integration output. The terms governing errors proportional to rates about perpendicular axes (gyro cross-axis error parameters) are presumed to be fixed for any given installation and are established under a one-time calibration process. Gyro rate bias errors, however, will continually drift slowly with time and hence, need to be updated on a continuous basis. Error estimates from the Kalman filter are used to continually correct the IMU velocity and attitude output.

The detailed mechanics for the optimal estimation algorithm for system state estimation through a combination of a state-propagation model, an observation model and observation data are based on standard Kalman filter methods, which are well described by Gelb (1999).

2.2 Overview of Kalman filter 2

Kalman filter 2 employs differenced carrier-phase data from GPS satellites to provide an independent attitude reference source. If $\boldsymbol{s}_j$ represents the unit vector, defined in an earth-fixed reference frame, pointing to the jth GPS satellite in space from the aircraft and $\boldsymbol{d}$ represents the vector that defines the

separation of the two GPS antennas, also expressed in an earth-fixed frame, then the component of $\boldsymbol{d}$ projected onto the unit sight vector represents the difference in path length for the signal to reach one antenna vs. the other, i.e.,

$$\Delta_j = \boldsymbol{s}_j^{\mathrm{T}} \boldsymbol{d}. \tag{15}$$

The different path lengths result in a shift in signal phase, ζ_j, according to the wavelength of the GPS carrier signal, λ,

$$\zeta_j = \Delta_j / \lambda. \tag{16}$$

However, carrier phase data from the GPS processor, φ_j, repeats for each cycle of the carrier wavelength, so there is an intrinsic ambiguity K_j representing the complete integer number of wavelengths that is initially unknown when trying to obtain the total path-length difference:

$$\zeta_j = \varphi_j + K_j. \tag{17}$$

The geometric solution for attitude Euler angles is implied by the transformation matrix $\boldsymbol{C}_{\mathrm{eb}}$ that maps the antenna baseline vector in the body frame, $\boldsymbol{r}_{\mathrm{b}}$, to the baseline vector in the inertial frame, i.e.,

$$\boldsymbol{d} = \boldsymbol{C}_{\mathrm{eb}}(\phi, \theta, \psi)\boldsymbol{r}_{\mathrm{b}}, \tag{18}$$

such that Eq. (15) is satisfied for all satellites j=1, 2,…, N given the set of GPS phase observations $\{\varphi_j\}$ and the set of phase ambiguity offsets $\{K_j\}$. Note that the set of ambiguity values $\{K_j\}$ should be constant once established unless there is a "cycle slip" in the tracking carrier-phase.

Kalman filter 2 takes the attitude state defined by the vector $[\phi, \theta, \psi, \dot{\phi}, \dot{\theta}, \dot{\psi}]^{\mathrm{T}}$ at t_n and projects it forward to t_{n+1} using a first-order integration stage,

$$\phi_{n+1} = \phi_n + \dot{\phi}_n \Delta t, \tag{19}$$

$$\theta_{n+1} = \theta_n + \dot{\theta}_n \Delta t, \tag{20}$$

$$\psi_{n+1} = \psi_n + \dot{\psi}_n \Delta t, \tag{21}$$

$$\dot{\phi}_{n+1} = \dot{\phi}_n, \tag{22}$$

$$\dot{\theta}_{n+1} = \dot{\theta}_n, \tag{23}$$

$$\dot{\psi}_{n+1} = \dot{\psi}_n. \tag{24}$$

The projected state parameters at t_{n+1} are then used to predict the measurement set at t_{n+1}, which includes attitude angles and attitude rates and the set of the latest GPS carrier-phase differences. Following standard Kalman filter algorithm design, discrepancies between the next set of observation data, from the IMU and GPS, and these predictions are used to refine the state vector in a manner that minimizes error variance.

3 Kalman filter 1 extensions

3.1 Accelerometer error modeling

In Section 2, factors affecting attitude error were considered alone in forming a mathematical model for IMU-velocity error propagation. In this model, attitude errors are mapped to velocity error behaviour through the effect these errors have on the IMU acceleration vector resolved into the earth-fixed reference frame. The Kalman filter seeks to find attitude error corrections necessary for observed accelerations in the body-fixed frame to remain consistent with observed GPS velocities. The IMU accelerometer triad is, therefore, the fundamental attitude reference.

It is difficult to determine accelerometer errors (e.g., bias offset, cross-axis rate sensitivity) when these accelerometers are themselves the primary source of attitude and velocity information. Without sufficiently redundant observation data for attitude, velocity or acceleration, it is possible for the filter solution to become unstable given the potential for positive feedback, e.g., an accelerometer error estimate affecting velocity error may cause a change in attitude error which then affects the accelerometer error estimate.

Acceleration measured in the IMU body-fixed frame was previously assumed to be error free and that any small biases would be manifest as small attitude offsets that would be handled by system flight-calibrations. Now we consider the implications of modelling accelerometer error following the model implemented for gyro errors wherein the sensor output is a combination of the true rate plus an initially unknown bias offset and cross-axis sensitivity, where components of acceleration perpendicular to the sensing axis affect sensor output, i.e.,

$$\hat{\boldsymbol{a}}_{\mathrm{b}} = \boldsymbol{a}_{\mathrm{b}} + \boldsymbol{\eta} + \boldsymbol{\mu}\boldsymbol{a}_{\mathrm{b}}, \tag{25}$$

where $\hat{\boldsymbol{a}}_{\mathrm{b}}$ is the sensor output based on the ideal perfect body acceleration $\boldsymbol{a}_{\mathrm{b}}$, a set of acceleration offsets $\boldsymbol{\eta}$ and cross-axis sensitivity expressed as a 3×3 matrix $\boldsymbol{\mu}$. The cross-axis sensitivity matrix is defined as

$$\boldsymbol{\mu}=\begin{bmatrix} 0 & \delta\psi_{a1} & -\delta\theta_{a1} \\ -\delta\psi_{a2} & 0 & \delta\phi_{a2} \\ \delta\theta_{a3} & -\delta\phi_{a3} & 0 \end{bmatrix}. \tag{26}$$

Each matrix element represents a perturbation angle for the sensing axis off the ideal perpendicular, expressed in radians, of accelerometer $a1$, $a2$ or $a3$. The original equation for acceleration error in the inertial (earth-fixed) frame, Eq. (11), is extended accordingly:

$$\delta\boldsymbol{a}=\left(\frac{\partial\boldsymbol{C}_{\mathrm{eb}}}{\partial\phi}\delta\phi+\frac{\partial\boldsymbol{C}_{\mathrm{eb}}}{\partial\theta}\delta\theta+\frac{\partial\boldsymbol{C}_{\mathrm{eb}}}{\partial\psi}\delta\psi\right)\boldsymbol{a}_{\mathrm{b}}+\boldsymbol{C}_{\mathrm{eb}}(\boldsymbol{\eta}+\boldsymbol{\mu}\boldsymbol{a}_{\mathrm{b}}). \tag{27}$$

The model for propagation of velocity error based on Eq. (10) is now dependent on the initially unknown parameters ($\delta\phi$, $\delta\theta$, $\delta\psi$), (P_0, Q_0, R_0), and the new quantities ($\boldsymbol{\eta}$, $\boldsymbol{\mu}$).

3.2 Estimation of GPS phase lag

At its core, the Kalman attitude filter extracts attitude information by comparing velocities from IMU accelerometer integration with velocity data in the earth-fixed frame from an independent source, namely, the GPS. The model presumes that any differences between these two velocities are due to errors attributable to the IMU rate integration process alone. However, GPS information is not error free.

GPS velocity is very accurate, with uncertainties of the AIMMS-20 processor boards with the standard-positioning service being less than a few cm/s. However, the existence of a finite time delay between each IMU velocity update and the latest GPS solution causes an effective velocity error, depending on the body acceleration. The propagation time from inertial excitation, to the sensor, through the analog electronics, digitization and final transmission across the CAN bus is much shorter than the IMU refresh cycle of time of 25 ms. The GPS solution, however, involves complex mathematical data reduction that will take an unknown amount of time that will likely vary depending of the number of satellites being incorporated into the solution. Properties of this filter are unknown as they are proprietary properties of the GPS board manufacturer.

Once the GPS navigation solution is available it is transmitted via a RS232 connection at 38.4 kbps to the AIMMS interface, then it is transmitted across the CAN bus at 500 kbps. The estimated time to transmit the data across the serial link is 20 ms and the time to forward it across the CAN bus is about 2 ms.

The solution refresh period on the GPS processors is 200 ms. If the internal GPS processing delay is some reasonable fraction of this, say 30%–40%, it is then possible for the combined time uncertainty between receipt of a GPS update at the main AIMMS processor and the latest IMU output cycle to be 125 ms or more. If the aircraft is executing a manoeuver, such as a moderately banked turn, it is possible for acceleration to be as much as 1g. The consequences of a 125 ms time lag in this instance would be in excess of 1 m/s in terms of velocity, which is close to two orders of magnitude worse than the accuracy of the GPS velocity itself. Clearly phase lag between the IMU and the GPS velocity reference has potentially important implications for attitude accuracy.

Earlier implementations of this algorithm handled GPS phase lag relative to the inertial data by deliberately lagging all inertial data using a circular buffer in order to match the GPS data. The size of the circular buffer, and hence the number of IMU integration cycles that the data is deliberately lagged, was established by means of a covariance analysis of IMU accelerations and time-differenced GPS velocities. However, this resulted in a one-time estimate with little knowledge of how the phase relationship might change under different circumstances.

Here we take a different approach to the problem wherein the time lag of the GPS velocity is regarded as an initially unknown state parameter for which the Kalman filter continuously refines estimated values. Here we apply a model to predict the GPS velocity measurement based on the velocity output from the IMU and the state parameters of the filter model, e.g., the IMU error vector and the GPS time lag. If the time lag is represented by δt_g then the predicted GPS velocity vector at time $t=t_n$ is given by IMU output at t_n

minus the predicted Kalman filter the IMU error vector, $\delta\boldsymbol{\vartheta}_n$, and a correction based on integration of the latest estimates for acceleration and jerk, i.e.,

$$(\boldsymbol{\vartheta}_{\mathrm{GPS}})_n=\boldsymbol{\vartheta}_i(t_n)-\delta\boldsymbol{\vartheta}_n-\boldsymbol{a}_n\delta t_g-\frac{1}{2}\dot{\boldsymbol{a}}_n\delta t_g^2. \tag{28}$$

The time-step $\Delta t=t_n-t_{n-1}$ is set by the GPS navigation solution refresh rate, which is 200 ms for the AIMMS-20 system installed on the Hong Kong J4100 aircraft. The IMU update cycle is 25 ms, so eight IMU updates span one GPS cycle. Consequently, the acceleration $\boldsymbol{a}_n$ used here for each GPS/Kalman update is based on the set of three mean accelerometer readings over the latest eight IMU data cycles. The jerk vector, $\dot{\boldsymbol{a}}_n$, is given by the slope of the line-of-best-fit (in a least-squares sense) over the same eight IMU accelerometer data cycles.

3.3 Improved application of GPS velocity

As discussed extensively in Section 2.1, Kalman filter 1 operates by analyzing the differences between the velocities derived from integrated IMU rates and GPS velocity. The GPS velocity output from a particular GPS processor refers to the velocity of the antenna, not the velocity of the processor. Moreover, the velocity required for filter 1 operation refers specifically to the velocity of the IMU in inertial space.

Earlier implementations of the Kalman filter handled the problem of deriving the GPS velocity at the IMU from data representing velocities at each antenna by simply averaging the two sets of velocity data. Simple averaging provides the effective GPS velocity that would be obtained by an antenna located at the intersection of the antenna baseline and the aircraft centreline, assuming that the antennas are located on the wings equally distant from the fuselage. This assumption is typically good since the IMU is located inside the fuselage. However, IMU velocity could be in error by varying amounts during times of non-zero yaw and pitch rates depending on the fore/aft distance from the antenna baseline.

A generalized scheme was implemented to refine how GPS velocities are combined to infer the effective GPS velocity at the IMU. 3D coordinates are now used to define the exact position of each antenna relative to the IMU. Basic kinematic relationships are then applied to deduce the velocity of the IMU from the velocities at each of two antennas at a generalized location on the airframe. This is expected to be a modest improvement during times when significant non-zero yaw rates occur, i.e., during moderate to steeply banked turns. For example, if the IMU is longitudinally displaced from the baseline midpoint by 5 m, and the aircraft is executing a turn with a 45° bank at 100 m/s true airspeed (TAS) resulting in a turn rate of 5–6 °/s, then the velocity error at the IMU would be about 0.5 m/s. Although small, it can still bias the corrections generated by the error-tracking filter as this would appear to be pure velocity error without this correction.

The position vector of any point on the aircraft relative to a reference point fixed in the earth frame can be described by a vector summation of the position of the origin of the aircraft body-fixed frame relative to this point and the position vector relative to the aircraft-fixed origin, i.e.,

$$\boldsymbol{r}_{\mathrm{e}}=\boldsymbol{r}_0+\boldsymbol{r}_{\mathrm{b}}, \tag{29}$$

where $\boldsymbol{r}_{\mathrm{b}}$ is the position relative to the aircraft-fixed origin, taken to be at the centre of the IMU, and $\boldsymbol{r}_0$ is the position of the origin relative to an arbitrary reference point fixed in the earth-frame of reference. By expressing the vector $\boldsymbol{r}_{\mathrm{b}}$ in the body-frame and $\boldsymbol{r}_0$ and $\boldsymbol{r}_{\mathrm{e}}$ in the earth-fixed frame and taking the time-derivative, we can obtain the following expression for velocity in the earth frame in terms of the motion of the IMU, the angular velocity (expressed in the aircraft frame), and the position of the point $\boldsymbol{r}_{\mathrm{b}}$ and the coordinate frame transformation (body-frame >earth-fixed frame),

$$\dot{\boldsymbol{r}}_{\mathrm{e}}=\dot{\boldsymbol{r}}_0+\boldsymbol{C}_{\mathrm{eb}}(\dot{\boldsymbol{r}}_{\mathrm{b}}+\boldsymbol{\omega}^{\times}\boldsymbol{r}_{\mathrm{b}}), \tag{30}$$

where $\boldsymbol{\omega}^{\times}$ defines the cross-product with the angular velocity defined in the body-frame,

$$\boldsymbol{\omega}^{\times}=\begin{bmatrix}0 & -\omega_3 & \omega_2\\ \omega_3 & 0 & -\omega_1\\ -\omega_2 & \omega_1 & 0\end{bmatrix}. \tag{31}$$

If we assume rigid body motion, then the time rate of change of the position coordinates in the

body-fixed frame is zero. Eq. (30) can thus be simplified for antenna 1 (port) position $\boldsymbol{r}_{b1}$ and antenna 2 (starboard) position $\boldsymbol{r}_{b2}$ to yield,

$$\dot{\boldsymbol{r}}_{e1} = \dot{\boldsymbol{r}}_0 + \boldsymbol{C}_{eb}\boldsymbol{\omega}^{\times}\boldsymbol{r}_{b1}, \tag{32}$$

$$\dot{\boldsymbol{r}}_{e2} = \dot{\boldsymbol{r}}_0 + \boldsymbol{C}_{eb}\boldsymbol{\omega}^{\times}\boldsymbol{r}_{b2}. \tag{33}$$

GPS velocities at antennas 1 and 2 can thus be combined knowing aircraft attitude, hence $\boldsymbol{C}_{eb}$, and pitch rate from the IMU alone (ω_2). By subtracting Eq. (32) from Eq. (33), it is possible to solve for ω_1 and ω_3 and then back-substitute to obtain $\dot{\boldsymbol{r}}_0$, the best combined estimate of the GPS velocity at the IMU given GPS velocities at two antennas at different locations on the airframe.

4 Kalman filter 2 extension

One important limitation of filter 2 is that it operates at the update frequency of the carrier-phase data from the GPS boards, which is only 5 Hz. Important discrepancies between the projected attitude and the IMU attitude over the 200 ms update period can occur simply because the prediction includes only the first-order term, i.e., it assumes that angular velocity is a constant over the integration period. Any contributions to attitude angles due to angular acceleration over 200 ms are not included in the state prediction. Under flight conditions with manoeuvres no more dramatic than those that occurs during shallow turns this approximation is very good. However, 200 ms is a long time to assume that angular rates are constant when executing more dynamic manoeuvres, such as those experienced when entering a steep turn. The "correction phase" of the filter, which reconciles differences between predicted and observed measurement data, can then misinterpret these prediction errors and adjust various aspects of the attitude solution. One possible approach to this problem is to assign a larger uncertainty to the prediction state model so that less "weight" is assigned to the predicted state. It was deemed better to improve the quality of the low-frequency attitude prediction stage by increasing the order of time integration by one, i.e., to explicitly track and include angular acceleration estimates.

Higher order integration is implemented by extending the attitude state vector: $[\phi,\theta,\psi,\dot{\phi},\dot{\theta},\dot{\psi},\ddot{\phi},\ddot{\theta},\ddot{\psi}]^{\mathrm{T}}$ and the state-prediction integration stage of the filter is extended according to the followings:

$$\phi_{n+1} = \phi_n + \dot{\phi}_n\Delta t + \frac{1}{2}\ddot{\phi}_n\Delta t^2, \tag{34}$$

$$\theta_{n+1} = \theta_n + \dot{\theta}_n\Delta t + \frac{1}{2}\ddot{\theta}_n\Delta t^2, \tag{35}$$

$$\psi_{n+1} = \psi_n + \dot{\psi}_n\Delta t + \frac{1}{2}\ddot{\psi}_n\Delta t^2, \tag{36}$$

$$\dot{\phi}_{n+1} = \dot{\phi}_n + \ddot{\phi}_n\Delta t, \tag{37}$$

$$\dot{\theta}_{n+1} = \dot{\theta}_n + \ddot{\theta}_n\Delta t, \tag{38}$$

$$\dot{\psi}_{n+1} = \dot{\psi}_n + \ddot{\psi}_n\Delta t, \tag{39}$$

$$\ddot{\phi}_{n+1} = \ddot{\phi}_n, \tag{40}$$

$$\ddot{\theta}_{n+1} = \ddot{\theta}_n, \tag{41}$$

$$\ddot{\psi}_{n+1} = \ddot{\psi}_n. \tag{42}$$

5 Wing flexure Kalman filter model

The 3D wind vector is derived from the wind measured in the aircraft-fixed frame, which is attached to the IMU located in the cabin. Orientation and velocity about the IMU, relative to earth-fixed reference frame, is used to transform this aircraft-relative wind (ARW) vector into the wind vector with respect to the earth frame. However, the ARW is resolved by the ADP mounted on the wing-tip of the Hong Kong GFS BAE J4100 aircraft. In the previous wind-data processing code, adjustments for the moment arm, i.e., separation of the probe from the IMU, were made assuming that the aircraft is a rigid body. The wing, however, is a flexible body and its structural response to dynamic loads will cause the velocity at the wing tip to differ from expectation according to the rigid-body model. Frequencies for which this effect will be important will be centred about the natural vibration frequency of the wing. The issue, therefore, is one of potential importance for resolving the 3D wind vector in the turbulence regime depending on wing stiffness.

The design of the Aventech ADP anticipated the potential needs to address the issue of flexible structures by incorporating an accelerometer triad with

other air-data sensors inside the ADP. The objective here is to examine and implement a possible processing algorithm and evaluate if wing motion relative to the IMU has any significant bearing on turbulence calculations for the J4100 aircraft.

A cantilevered wing is very stiff in the chord-wise direction and least stiff in the direction normal to the wing plane. Torsional stiffness lies between these extremes and can potentially play a role by changing the pitch orientation of the probe relative to the IMU. However, the twisting response of a wing to varying wing loads is a matter of significant concern to airworthiness as torsional bending can increase the local angle of attack, thereby increasing aerodynamic loads that increase torsional bending further. This can lead to the unstable aero-elastic response of flutter and, in the worst-case, to complete structural failure. Torsional bending, therefore, is guaranteed by the flight certification process to be very small relative to normal angle-of-attack variations of the wing. As a result, a decision was made to first examine possible effects of the dominant source of structural bending alone: up/down wing-tip deflections due to bending in response to lift acting normal to the wing surface.

The model formulation assumes that the IMU is located at a point P_1 in the fuselage and the ADP is located at point P_2 near the wing tip (Fig. 2).

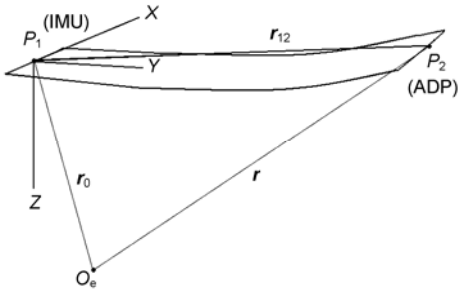

Fig. 2 Wing flex geometry

Point O_e is an arbitrary reference point in the earth-fixed reference frame. The position in inertial space of the ADP (P_2) is then represented by the sum of vectors defining the position of the probe relative to the IMU, $\boldsymbol{r}_{12}$, and the position of the IMU relative to the earth-fixed frame, $\boldsymbol{r}_0$. Wing flexure is modelled by introducing the variable $\boldsymbol{d}$ that defines the distance that the probe has moved from its rest position in the aircraft/IMU-fixed reference frame. It is assumed that displacement due to flex will be effectively perpendicular to vector $\boldsymbol{r}_{12}$. The vector defining this displacement is then given by the product $\boldsymbol{n}$, where $\boldsymbol{n}$ is defined as the unit normal vector to the wing plane (Fig. 3).

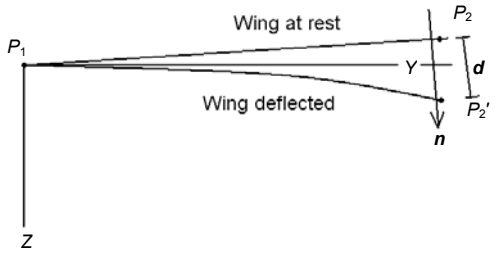

Fig. 3 Definition of wing flex parameters

The position of the wing tip in the inertial frame is then described by

$$\boldsymbol{r} = \boldsymbol{r}_0 + \boldsymbol{r}_{12} + \Delta\boldsymbol{r}, \tag{43}$$

where

$$\Delta\boldsymbol{r} = \mathrm{d}\boldsymbol{n}. \tag{44}$$

Eq. (43) is differentiated once to obtain the velocity of the wing tip in the earth-fixed frame. Vector quantities in Eq. (43) can be expressed as coordinate column-matrices with respect to two different reference frames: $\boldsymbol{r}$ and $\boldsymbol{r}_0$ are defined relative to the earth-fixed frame, and $\boldsymbol{r}_{12}$ and $\Delta\boldsymbol{r}$ are defined relative to the IMU-fixed reference frame attached to the aircraft. The time derivative of Eq. (43) can then be expressed in terms of these components according to

$$\dot{\boldsymbol{r}} = \dot{\boldsymbol{r}}_0 + \boldsymbol{C}_{\mathrm{e1}}[(\dot{\boldsymbol{r}}_{12} + \Delta\dot{\boldsymbol{r}}) + \boldsymbol{\omega}^{\times}(\boldsymbol{r}_{12} + \Delta\boldsymbol{r})], \tag{45}$$

where $\boldsymbol{C}_{\mathrm{e1}}$ is defined as the rotational transformation matrix to convert coordinates in the IMU frame to the earth-fixed reference frame and the cross-product matrix of angular velocity components in the body frame. By taking the time-derivative once more of Eq. (45) and noting that time derivatives of $\boldsymbol{r}_{12}$ are identically zero as prescribed by the model, we can obtain the following expression for acceleration of the P_2 in the inertial frame:

$$\begin{aligned}\ddot{\boldsymbol{r}} = \ddot{\boldsymbol{r}}_0 + \boldsymbol{C}_{\mathrm{e1}}[&(\Delta\ddot{\boldsymbol{r}} + 2\boldsymbol{\omega}^{\times}\Delta\dot{\boldsymbol{r}} + \dot{\boldsymbol{\omega}}^{\times}(\boldsymbol{r}_{12} + \Delta\boldsymbol{r}) \\ &+ \boldsymbol{\omega}^{\times}\boldsymbol{\omega}^{\times}(\boldsymbol{r}_{12} + \Delta\boldsymbol{r})],\end{aligned} \tag{46}$$

where $\ddot{\boldsymbol{r}}_0$ is the acceleration of the IMU in the earth-frame, $\Delta\ddot{\boldsymbol{r}}$ is the acceleration of ADP in a direction normal to the wing plane, $2\boldsymbol{\omega}^{\times}\Delta\dot{\boldsymbol{r}}$ is the coriolis acceleration, $\dot{\boldsymbol{\omega}}^{\times}(\boldsymbol{r}_{12}+\Delta\boldsymbol{r})$ is the angular acceleration, and $\boldsymbol{\omega}^{\times}\boldsymbol{\omega}^{\times}(\boldsymbol{r}_{12}+\Delta\boldsymbol{r})$ is the centripetal acceleration.

Now that as probe acceleration has been defined in terms of its position relative to the IMU and its displacement normal to the reference wing plane, it is possible to express acceleration data that should be output from the ADP accelerometer triad. This requires us to define the additional reference frame $\mathcal{F}_2$, which is attached to the ADP. $\mathcal{F}_2$ is assumed to be aligned parallel to the IMU frame attached to the aircraft, $\mathcal{F}_1$, but with a roll offset, i.e.,

$$\phi_{\text{probe}}=\phi_{\text{IMU}}+v_0+\delta v, \tag{47}$$

where v_0 is the equilibrium roll-offset angle and δv is the change in roll angle associated with wing bending from the rest position. Note that the wing is assumed to be perfectly rigid in torsion and fore/aft directions, but can bend only in the up/down direction defined by the unit normal vector $\boldsymbol{n}$. The associated small roll-deflection angle δv will not affect the angle of incidence of the probe and, therefore, will not affect flow angles resolved by the probe. The parameter is included purely to model accelerometer response to this motion.

The ideal accelerometer signal, $\boldsymbol{a}_2$, defined in $\mathcal{F}_2$ without internal bias offsets or cross-axis error sensitivity is then derived from the probe acceleration defined in the earth frame by applying a rotational transformation from the earth frame to the probe frame, $\boldsymbol{C}_{2\text{e}}$:

$$\boldsymbol{a}_2=\boldsymbol{C}_{2\text{e}}(\boldsymbol{a}_{\text{e}}-g\hat{\boldsymbol{e}}_3). \tag{48}$$

Accelerometers sense acceleration by measuring the body force acting upon a test mass, with gravity being indistinguishable from the inertial force due to acceleration. Gravity appears to the sensor to be an inertial reaction force caused by acceleration in the opposite direction. Consequently, gravity is accounted in modelling sensor output by reversing the sign of its contribution before adding it to the true acceleration, as shown in Eq. (48), where $\hat{\boldsymbol{e}}_3$ is defined as the z unit coordinate vector of the earth frame that points towards the centre of the earth.

Accelerometer output including sensor bias and cross-axis terms is modelled according to

$$\hat{\boldsymbol{a}}_2=\boldsymbol{\eta}+(\boldsymbol{I}+\boldsymbol{\mu})\boldsymbol{a}_2, \tag{49}$$

where $\boldsymbol{I}$ is defined as the 3×3 identity matrix. Upon substitution of Eq. (46) into Eq. (48), noting that $\boldsymbol{a}_{\text{e}}=\ddot{\boldsymbol{r}}$, we can obtain the following equation for the modeled ADP accelerometer output,

$$\begin{aligned}\hat{\boldsymbol{a}}_2=\boldsymbol{\eta}+(\boldsymbol{I}+\boldsymbol{\mu})\boldsymbol{C}_{21}[&\boldsymbol{C}_{1\text{e}}\ddot{\boldsymbol{r}}_0+\Delta\ddot{\boldsymbol{r}}+2\boldsymbol{\omega}^{\times}\Delta\dot{\boldsymbol{r}}\\&+\dot{\boldsymbol{\omega}}^{\times}(\boldsymbol{r}_{12}+\Delta\boldsymbol{r})+\boldsymbol{\omega}^{\times}\boldsymbol{\omega}^{\times}(\boldsymbol{r}_{12}+\Delta\boldsymbol{r})-g\boldsymbol{C}_{1\text{e}}\hat{\boldsymbol{e}}_3],\end{aligned} \tag{50}$$

after making use of the following relationship for rotational transformation matrices:

$$\boldsymbol{C}_{21}=\boldsymbol{C}_{2\text{e}}\boldsymbol{C}_{\text{e}1}. \tag{51}$$

The general rotational transformation between the aircraft-fixed IMU frame 1 and the ADP-fixed frame 2 is given by the following matrix, where frame 2 is rolled about the x axis by (v_0+δv) relative to frame 1:

$$\boldsymbol{C}_{21}=\begin{bmatrix}1&0&0\\0&\cos(v_0+\delta v)&\sin(v_0+\delta v)\\0&-\sin(v_0+\delta v)&\cos(v_0+\delta v)\end{bmatrix}. \tag{52}$$

5.1 Kalman filter state model

The state vector characterizing the wing flexure problem is defined by the wingtip displacement $\boldsymbol{d}$ and its derivatives, and the tip roll offset δv plus terms related to the accelerometer error model. The filter state vector $\boldsymbol{\chi}$ is defined by

$$\boldsymbol{\chi}=[d,\dot{d},\ddot{d},\delta v,\gamma,\eta_1,\eta_2,\eta_3,\delta\theta_{a1},\delta\psi_{a1},\delta\phi_{a2},\delta\phi_{a3},\delta\theta_{a3}]^{\text{T}}, \tag{53}$$

where γ is a constant of proportionality between ADP rotation and the tip deflection due to wing bending, the three η terms represent the set of three accelerometer biases, and the six δ terms represent cross-axis

error sensitivity for accelerometers $a_1(x)$, $a_2(y)$ and $a_3(z)$.

The state transition model, which predicts the state $\boldsymbol{\chi}$ at t_{n+1} from the state $\boldsymbol{\chi}(t_n)$ as part of the filter update process, is given as

$$d_{n+1} = d_n + \dot{d}_n \Delta t + \frac{1}{2}\ddot{d}_n \Delta t^2, \tag{54}$$

$$\dot{d}_{n+1} = \dot{d}_n + \ddot{d}_n \Delta t, \tag{55}$$

$$\ddot{d}_{n+1} = \ddot{d}_n, \tag{56}$$

$$\delta v_{n+1} = \delta v_n + \gamma_n \left(\dot{d}_n \Delta t + \frac{1}{2}\ddot{d}_n \Delta t^2 \right), \tag{57}$$

$$\chi_{5-14,\, n+1} = \chi_{5-14,\, n}. \tag{58}$$

Eq. (57) can be interpreted as requiring that the change in the tip deflection angle should be proportional to the change in wingtip deflection, with the constant of proportionality, γ, to be estimated as part of the filter state vector.

5.2 Kalman measurement vector

Three accelerometer channel outputs from the ADP comprise the only sensor inputs to the wing-flex filter. One additional virtual measurement was included with the measurement vector: the wing displacement $\boldsymbol{d}$. This is assigned a measurement value of zero at all times to act as a constraint on wing-tip motions. Without such a constraint, there would be nothing from preventing a small accelerometer bias from causing the wing tip to continually accelerate up or down relative to the IMU without limit.

The wing structure will always oppose any dynamically-applied force causing structural bending. Over time, the mean deflection will approach the value it achieves in static equilibrium, specifically $\boldsymbol{d}$=0. The Kalman formulation, however, allows the state estimate for $\boldsymbol{d}$ to assume a range of values centred about this input value, or "virtual measurement", consistent with prescribed statistical properties.

Each term in the measurement vector is assumed to be the sum of the "true" measurement plus Gaussian noise with zero mean and a known variance. By specifying a small variance, each value is assigned a higher weight and state parameters dependent upon such measurements will be quickly "pulled" toward the observation. However, any measurement with a large variance assigned for noise will have a much smaller impact on closely related state variables on each filter update cycle.

The filter can ensure the mean tip displacement approaches zero with this virtual measurement input. By prescribing a sufficiently large variance for the virtual measurement $\boldsymbol{d}$=0, however, it is possible to do this without adversely attenuating real motions demanded by the accelerometer measurements. Numerical experiments were performed to verify a variance setting that ensures the mean displacement seeks zero but without excessively damping the response function $\boldsymbol{d}(t)$.

6 Temperature sensor lag correction

Air temperature measurement poses a few challenges when the speed of the flow becomes large as is the case for the BAE J4100 for which airspeed can be in excess of 100 m/s. The energy implicit to high velocities can cause damage to the small and delicate (0.040″ diameter) thermistor sensing element if it is not properly protected. Moreover, flow energy in the form of pressure or kinetic energy can modify the temperature of the flow itself.

The AIMMS-20 ADP employs a reverse-flow housing design that utilizes the principle of inertial separation to prevent particulate matter (insects, rain, ice crystals, dust, etc.) from entering the ventilation tube and damaging the thermistor or causing sensor wetting in the case of water droplets. The flow is slowed down considerably as it separates and stagnates about the rear-facing ventilation tube inlet. Pressure recovery resulting from this manipulation of the flow is 70% of the total dynamic head according to wind tunnel investigations. Corrections are applied to the temperature output based on the known TAS and this recovery factor. TAS reduction is performed using the corrected temperature value from the previous data cycle. On the first cycle, uncorrected temperature data is used in place of the true air temperature for the purpose of TAS calculation. This iteration rapidly converges as air temperature has only a small effect on TAS, introducing less than 0.2% error per degree at 0 °C.

Flow manipulation by slowing and drawing it through a rear-facing ventilation tube has one undesirable side-effect: it introduces thermal mass into the flow circuit that affects the temperature response of

the system as a whole. The 0.040″ thermistor element has a response time in moving air that is much less than 1 s. However, the observed response of the ADP temperature output indicates a much longer response time. Clearly the thermal behaviours of the ADP structure and thermistor housing are having an effect on temperature data.

A sensor model was constructed to estimate the combined response of the sensor and housing, and a correction algorithm based on this model was implemented and tested.

6.1 Sensor response model

A diagrammatic representation of how the flow is managed by the temperature/humidity sensor housing is shown in Fig. 4.

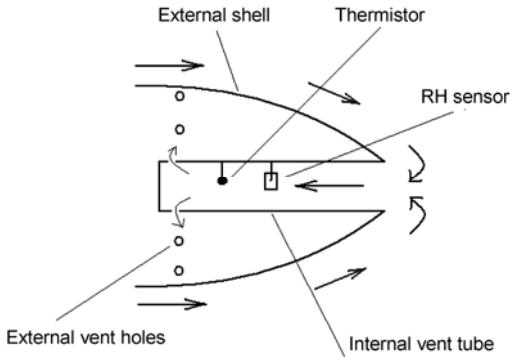

Fig. 4 Temperature/relative humidity (RH) sensor housing

Heat will be transferred from the external shell to the thermal boundary layer of the external flow. Similarly, heat will be transferred from the walls of the internal vent tube into the ventilating flow. Since the flow is turbulent, beginning with flow separation near the aft of the probe, it is expected that heat transferred from the walls will be well mixed into the ventilating flow.

The following assumptions were made in formulating the temperature response model:

1. The rate of change of temperature of the thermistor, T, with time is proportional to the difference between the thermistor temperature and the ventilating flow temperature T_v.

2. The ventilating tube/enclosure effect can be represented by a single characteristic temperature T_E.

3. Heat flux into the ventilating flow from the housing material is proportional to the difference between T_E and the air temperature T_A.

4. The rate of change of the enclosure temperature is proportional to the difference between it and the external air temperature.

Expressed mathematically, assumption 1 becomes:

$$\frac{\mathrm{d}T}{\mathrm{d}t}=-\lambda_\mathrm{s}(T-T_\mathrm{v}). \tag{59}$$

The temperature rise of the ventilating flow over the ambient air temperature is obtained by combining assumptions 2 and 3:

$$T_\mathrm{v}-T_\mathrm{A}=-\alpha(T_\mathrm{A}-T_\mathrm{E}). \tag{60}$$

Following Eq. (59) and applying assumption 4, the characteristic enclosure temperature is related to the air temperature by

$$\frac{\mathrm{d}T_\mathrm{E}}{\mathrm{d}t}=-\lambda_\mathrm{e}(T_\mathrm{E}-T_\mathrm{A}). \tag{61}$$

In essence, Eq. (60) shows that the temperature elevation of the ventilation flow is a constant fraction of the elevation temperature of the enclosure with respect to the air. This equation can be substituted into Eq. (59) to give the thermistor temperature in terms of the temperature of the air and enclosure:

$$\frac{\mathrm{d}T}{\mathrm{d}t}=-\lambda_\mathrm{s}(T-(1-\alpha)T_\mathrm{A}-\alpha T_\mathrm{E}). \tag{62}$$

Upon taking the Fourier transform (denoted by the operator $\Im$) of Eq. (62), using iω to denote complex frequency, we obtain

$$(\mathrm{i}\omega+\lambda_\mathrm{s})\Im(T)=\lambda_\mathrm{s}(1-\alpha)\Im(T_\mathrm{A})+\lambda_\mathrm{s}\alpha\Im(T_\mathrm{E}). \tag{63}$$

Similarly, by taking the Fourier transform of Eq. (61):

$$(\mathrm{i}\omega+\lambda_\mathrm{e})\Im(T_\mathrm{E})=\lambda_\mathrm{e}\Im(T_\mathrm{A}). \tag{64}$$

Between Eqs. (64) and (63) it is possible to eliminate the enclosure temperature leaving the thermistor temperature in terms of the air temperature, specifically

$$\Im(T)=\frac{\lambda_s(1-\alpha)}{(\lambda_s+\mathrm{i}\omega)}\Im(T_A)+\frac{\alpha\lambda_s\lambda_e}{(\lambda_s+\mathrm{i}\omega)(\lambda_e+\mathrm{i}\omega)}\Im(T_A). \quad (65)$$

The transfer function $H(\omega)$ is defined as the ratio of system response output to the system input in the frequency domain by means of Fourier transforms, i.e., $H(\omega)=\Im(\text{output})/\Im(\text{input})$. Taking the thermistor temperature as the system output and the air temperature as the system input, this definition results in the following:

$$\Im(T)=H(\omega)\Im(T_A). \quad (66)$$

Eq. (66) can be inverted to obtain the air-temperature input as a function of the thermistor temperature output,

$$\Im(T_A)=H^{-1}(\omega)\Im(T). \quad (67)$$

Taking the inverse Fourier transform then recovers what we set out to obtain from the beginning of the section through a process called a de-convolution. The air temperature signal free of lag error is then given by the following de-convolution:

$$T_A=\Im^{-1}(H^{-1}(\omega)\Im(T)), \quad (68)$$

where the inverse system transfer function is as

$$H^{-1}(\omega)=\left(\frac{\lambda_s(1-\alpha)}{(\lambda_s+\mathrm{i}\omega)}+\frac{\alpha\lambda_s\lambda_e}{(\lambda_s+\mathrm{i}\omega)(\lambda_e+\mathrm{i}\omega)}\right)^{-1}. \quad (69)$$

When α=0, Eq. (65) becomes a function of the thermistor response only, i.e., the effect of the enclosure temperature response becomes irrelevant. When α=1, Eq. (65) becomes a function of both the enclosure and thermistor response functions with the individual response transfer functions multiplied together, as if acting in a cascade, i.e., the output from one process (enclosure modification of inlet air temperature setting the ventilation flow temperature) becomes the input for the next (thermistor response to ducted ventilation flow temperature). Hence, the transfer functions multiply together.

Lag-corrected temperature T_A requires appropriate values for the set of three parameters: λ_s, λ_e and α, i.e., thermistor time-response, enclosure time-response and the proportionality constant, respectively, defining the influence of the enclosure on thermally biasing the ventilating airflow in contact with the thermistor. Unfortunately, of these three parameters only the time-response for the thermistor is remotely known. An optimal parameter estimation scheme was devised to estimate reasonable values for λ_e and α from calibration flight data. The estimation algorithm is discussed below.

6.2 Estimation algorithm: enclosure temperature-response parameters

The epoxy micro-bead thermistor time-constant is a few 0.1 s, which improves with ventilation velocity. For time constant values <<1 s, absolute temperature lag magnitude is very small. For example, an aircraft climbing at a rate of 1000 fpm (5.08 m/s) through an adiabatic layer will experience a temperature change rate of −0.05 °C/s, which means that the steady-state lag will be −0.005 °C for 0.1 s time constant. Thus, small uncertainties for this term (e.g., 0.2 s vs. 0.1 s) will have very little absolute impact.

In contrast, the significant thermal mass of the enclosure ensures significant potential for much larger effects. It is for this reason that the time constant for the ventilated thermistor was held fixed, at an assumed constant value of 0.1 s (λ_s=10), and only λ_e and α were subject to parameter estimation analysis from flight data.

If we represent the true temperature signal by the set of data points $\{T_i\}$ and the de-convolved estimate by the set $\{T_i'\}$, then it is possible to construct a cost function S to be minimized by proper selection of λ_e and α. Following standard least-squares minimum variance schemes, the cost function S is defined as

$$S=\sum\nolimits_i(T_i'-T_i)^2. \quad (70)$$

Since $\{T_i'\}$ are derived by a de-convolution based on values λ_e and α, the cost function may be considered a function of these two parameters, i.e., $S=S(\lambda_e, \alpha)$. At the point at which the function S achieves a minimum value we must also have the two partial derivatives simultaneously equal to zero. From Eq. (70), this results in the following system of equations:

$$\sum_i (T_i' - T_i)\frac{\partial T'}{\partial \lambda_e} = 0, \tag{71}$$

$$\sum_i (T_i' - T_i)\frac{\partial T'}{\partial \alpha} = 0. \tag{72}$$

Terms $\frac{\partial T'}{\partial \lambda_e}$ and $\frac{\partial T'}{\partial \alpha}$ can be evaluated by taking partial derivatives of the inverse transfer function with respect to λ_e and α before computing the inverse Fourier transform (Eq. (68)).

To obtain a solution to Eqs. (71) and (72), it is convenient to define the following vector function:

$$\boldsymbol{G}(\boldsymbol{X}) = \begin{bmatrix} \sum_i (T_i' - T_i)\frac{\partial T'}{\partial \lambda_e} \\ \sum_i (T_i' - T_i)\frac{\partial T'}{\partial \alpha} \end{bmatrix} = 0,\ \boldsymbol{X} \equiv \begin{bmatrix} \lambda_e \\ \alpha \end{bmatrix}. \tag{73}$$

So the optimal solution of the following equation is zero:

$$\boldsymbol{G}(\boldsymbol{X})=\boldsymbol{0}. \tag{74}$$

A Newton-iteration was implemented to solve for the root according to

$$\Delta \boldsymbol{X}_i = -\left[\frac{\mathrm{d}\boldsymbol{G}}{\mathrm{d}\boldsymbol{X}}\right]^{-1} \boldsymbol{G}(\boldsymbol{X}_i), \tag{75}$$

$$\boldsymbol{X}_{i+1}=\boldsymbol{X}_i+\Delta \boldsymbol{X}_i. \tag{76}$$

Note: the 2×2 matrix $\frac{\mathrm{d}\boldsymbol{G}}{\mathrm{d}\boldsymbol{X}}$ consists of partial derivatives of quantities involving inverse Fourier transforms without any analytic closed form for evaluation. Consequently, the partial derivatives of Eq. (75) are evaluated numerically by finite-differencing.

7 Validation of Kalman filter extensions

Improvements to the Kalman filter attitude solver constitute fine-tuning adjustments to the process by which acceleration and angular rate information from the IMU are fused together and reconciled against the GPS velocities measured for the two wing-tip mounted antennas. In summary, the following algorithm improvements were made: (1) Accelerometer error modeling; (2) Incorporation of an explicit GPS phase-lag that is continually tracked and updated; (3) More precise handling of GPS velocity data from the wing tips to estimate GPS velocity at the IMU in the fuselage; and (4) Increasing the order of integration to improve precision of the differential carrier-phase algorithm to compensate for the fact that it runs at only 5 Hz.

The Kalman filter algorithm advances in two stages, functioning as a "predictor-corrector" scheme: the first stage takes the current state estimate and all that is known about system behaviour to predict the state at the next time step. The second stage applies observations of the system at the next time step to refine the predicted state. This is accomplished by predicting the measurements that should result from the predicted state and comparing these against a set of real observations. In this manner, the filter not only combines knowledge of the system based on a set of measurements, but also makes full use of everything that is known about how the system should behave. The "corrector" stage of the process first evaluates what is called a residual vector, which is the difference between the latest set of measurements and the predicted values based on the system model.

If the state behaviour model, sensor behaviour model and the measurements themselves were perfect, then all elements of the residual vector would be zero. Non-zero residual values indicate imperfections in state estimates necessitating refinement by the filter "corrector" stage. The behaviour of the residual is, therefore, indicative of the quality of the state and measurement models.

Behaviour of velocity measurement residuals was used as the basis to gauge the success of the above improvements. A system calibration flight was flown by the Hong Kong GFS on Nov. 26, 2009 that consisted of a pair of reciprocal flight tracks followed by a series of three 360° orbits at progressively steeper bank angles (15°, 30° and 45°), followed by a series of similar orbits but in the opposite direction. Rolling into turn, banking the aircraft and accelerating about a circular arc introduce important accelerations. It is during periods such as these that we expect any small discrepancies in how acceleration and velocity data are handled to reveal themselves. Fig. 5 illustrates the behaviour of the north-velocity

component residual (the GPS velocity estimated at the IMU–the velocity prediction from IMU rate integration+Kalman filter) based on the old filter formulation (red line) and the filter formulation with all above revisions (black line). True heading is superimposed, and referenced against the right *y* axis, to provide context with regard to aircraft manoeuvres.

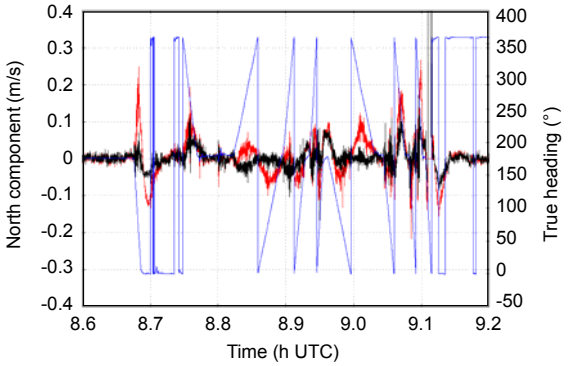

Fig. 5 North-velocity component residual before and after algorithm upgrades on the Nov. 26, 2009 Flight by GFS J4100

The blue line represents the true heading, the red line and black line represent the before and after algorithm upgrades, respectively (Note: for interpretation of the references to color in this figure legend, the reader is referred to the web version of this article)

A few observations are immediately apparent. Firstly, the two residual curves were almost identical during steady flight. Secondly, during periods of acceleration in turns, the previous algorithm implementation exhibited oscillatory residual errors that were typically larger in amplitude by a factor of about 2. Similar behaviour was exhibited for the east vector component as shown in Fig. 6.

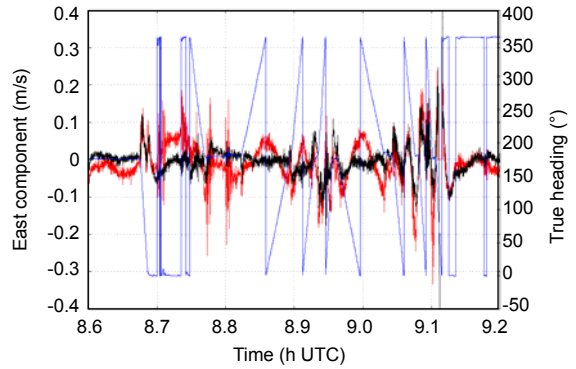

Fig. 6 East-velocity component residual before and after algorithm upgrades on the Nov. 26, 2009 Flight by GFS J4100

This figure used the same representations as in Fig. 5

Here the improvement is somewhat more striking during the north-south calibration flight-legs. The east component is perpendicular to the flight direction and is more sensitive to small side-to-side velocity changes such as those occurring during the two sideslip manoeuvres executed on each leg. The two pairs of sideslips are clearly indicated by the small oscillation in heading, with one pair along the north flight leg occurring at about 8.70–8.75 h UTC followed by another pair of sideslips on the south leg ending just after 8.80 h UTC. There is a burst of residual error evident with the old algorithm that is almost totally absent with the new implementation during these manoeuvers.

These residual values represent the magnitude of unaccounted velocity error that has accumulated between GPS velocity updates, i.e., velocity error evolution over a 200 ms period. The values are small, but some with the old model peak at values in excess of 30 cm/s. This is not a great deal in terms of mean wind calculations, but velocity error of this magnitude and at high frequencies, will affect turbulence output as inertial velocity error translates directly into wind vector component error.

The residual for the vertical velocity is given by Fig. 7. Here we see very little in terms of oscillations that move significantly outside of the noise band. The most significant feature of this plot is the clear bias on the vertical velocity. This is a result of the previous model formulation not including a term for accelerometer bias. Thus, a continuous vertical acceleration error is manifested as a small velocity error offset when accumulated over 200 ms before the next Kalman filter cycle. The recent modifications, including accelerometer bias, have clearly removed this error. Again, the magnitude is small compared to the over-all mean wind accuracy specification of 50 cm/s, but an anomaly of a few cm/s at high frequencies will contribute to turbulence error.

Fig. 8 shows the GPS phase lag estimation for the same flight (Nov. 26, 2009). The lag estimate averages about 70 ms, with values ranging from 40–45 ms to as high as 120 ms. Without an independent source to confirm this behaviour, it is difficult to know how much of this is real and how much might be a function of the Kalman filter reconciling other errors and falsely biasing the lag estimate. In the approach used in the old filter formulation, the GPS

lag was set to a constant of 100 ms and indications were that this estimate was a little large. Consequently, it is not surprising to see a mean lag value of 70 ms in this context.

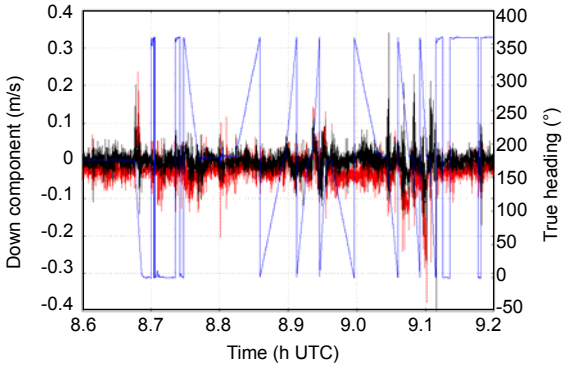

Fig. 7 Vertical-velocity component residual before and after algorithm upgrades on the Nov. 26, 2009 Flight by GFS J4100
This figure used the same representations as in Fig. 5

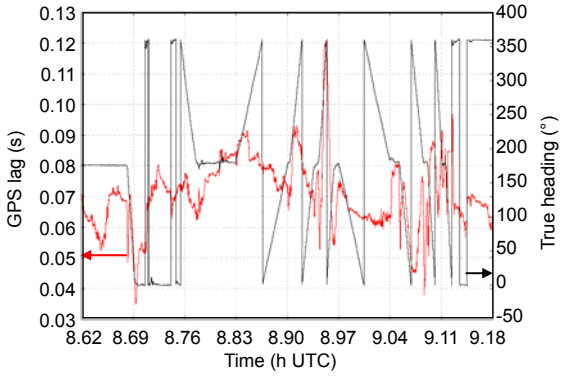

Fig. 8 Estimated GPS lag on the Nov. 26, 2009 Flight by GFS J4100

Part of the mean wander exhibited by the lag estimate, from 60 ms up to 85 ms then back down to 60 ms, could be due to slowly shifting phase between IMU updates and the arrival of GPS solutions, which trigger each Kalman filter cycle. The granularity of each IMU refresh is 25 ms, so it is possible for the GPS-triggered analysis cycle to fall anywhere within each 25 ms time-slice and the IMU velocity would not be able to reflect this fact. Therefore, given the design of the system and previous expectation, the results here are acceptable.

Finally, the impact of increasing the integration order for Kalman filter 2 is best demonstrated by the pitch-angle residual, i.e., the difference between the projected pitch angle and the value supplied as input by IMU integration. This is more significant than roll and true heading because carrier-phase data provide information to solve for these two modes as the antennas are mounted laterally on the GFS J4100. Indeed, this is the purpose of this filter, i.e., to fine-tune roll and true heading estimation using the high-precision GPS phase data. However, rate integration using IMU information is all that is available to generate pitch estimates by filter 2. Moreover, pitch error that might result from this coarse time-step size can potentially introduce error elsewhere due to the complex inter-relationships implicit to the rotational transformation between reference frames, specifically the transformation of the antenna baseline vector into inertial space. The 5 Hz integration rate was a concern that was addressed. Fig. 9 illustrates the pitch residual during filter 2 operation. The residual associated with the old algorithm is a measure of the inconsistencies between the 5 Hz integration update and the 40 Hz IMU process output used as an input.

The difference in performance as indicated by residual error is quite dramatic. It is clear that a significant improvement has been made with this update on how pitch it handled with the 5 Hz phase Kalman filter.

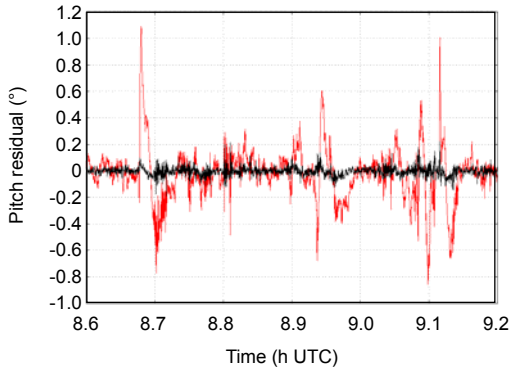

Fig. 9 Kalman filter 2 pitch residual before and after algorithm upgrades on the Nov. 26, 2009 Flight by GFS J4100
The red and black lines represent before and after algorithm upgrades, respectively (Note: for interpretation of the references to color in this figure legend, the reader is referred to the web version of this article)

8 Validation of wing-flex Kalman filter model

The wing-flexure model reconciles accelerometer output from the wing-tip mounted ADP with acceleration data from the IMU as discussed in Section 5. Data during the calibration flight of Nov. 26,

2009 was used to establish the general characteristics of the new algorithm. Fig. 10 shows the filter output for wing-tip displacement as a function of time.

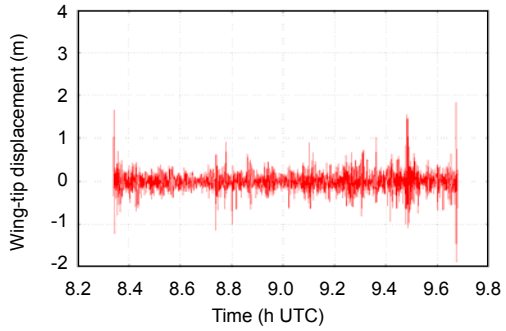

Fig. 10 Flex-induced wring-up vertical displacement in aircraft frame on the Nov. 26, 2009 Flight by GFS J4100

Statistics for displacement from the neutral position for the complete flight, from take-off to landing, were computed with the mean being −0.008 m and a root-mean-square (RMS) value of 23 cm. A small mean confirms the model formulation that specifies that the mean tip deflection is zero. A very small offset is most likely due to noise not integrating out completely to zero. With a semi-span of about 9 m, an RMS displacement of 23 cm normal to the chord plane is equivalent to an effective rotation about the wing root of 1.5°, which is an amount that is quite reasonable as this is a small fraction of the wing dihedral of 6.5°.

Spectral properties of wing motion output from the Kalman filter were examined by taking the fast Fourier transform (FFT) of tip acceleration data, i.e., the second derivative with respect to time of the tip deflection defined in the aircraft-fixed reference frame. Acceleration was selected as the basis for this analysis as acceleration is directly proportional to structural forces and should, therefore, be the most direct indicator of structural response. This spectrum was computed using 8192 points spanning 3.4 min of flight data during straight-level flight 500 s after take-off (Fig. 11).

This spectrum shows very clear evidence of a well-defined peak at about 4 Hz. Such behaviour is to be expected as the wing structure will possess a natural frequency at the first (fundamental) bending mode that will produce a defined spectral peak due to resonance. Although published data for the natural frequencies of wing vibration modes are not readily

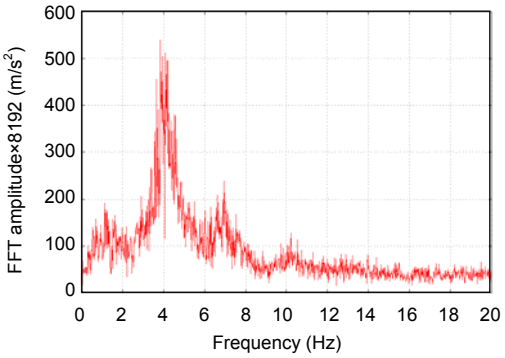

Fig. 11 Spectrum of wing-tip acceleration in aircraft-fixed frame on the Nov. 26, 2009 Flight by GFS J4100
8192-point FFT of 40 Hz data, 550 s from start of flight

available we can use, for example, data corresponding to an aircraft with a thin wing section and similar size: the Embraer (EMB) 145. The natural frequency of the first symmetric bending mode of the EMB 145 is 6.18 Hz (Rodrigues and Kamiyama, 1997). Thus, a fundamental frequency of 4 Hz is very much in the ball-park of what may be considered reasonable. The reason for modelling motion due to wing flexure is to improve the quality of probe inertial motion data to better resolve atmospheric turbulence.

It is well-known that the magnitude of the power spectrum of atmospheric turbulence decreases with the characteristic length scale of a turbulent eddy in proportion to $k^{-5/3}$, where k is the wave number. The wave number can be related directly to the frequency at which the turbulent eddies are encountered by the aircraft, so the power spectrum as a function of frequency f observed at the aircraft will similarly decrease in direct proportion to $f^{-5/3}$. Behaviour of aircraft turbulence observations relative to this well-established rule can be best extracted by plotting turbulence power E vs. frequency on a log-log basis. Taking the logarithm of both sides we can obtain:

$$\log E=\text{Const.}(-5/3)\log f. \tag{77}$$

Consequently, the slope of a line-of-best-fit through the spectral data converted to a log-log basis should be ideally −5/3.

The power spectrum was computed from 20 Hz wind data evaluated both with and without wing-flexure velocity calculations in effect. The spectrum was computed using a 4096-point FFT, with data spanning a period of 3.4 min during the calibration

flight of Nov. 26, 2009. This interval was chosen to coincide with circuit altitude near the end of the flight, as greater turbulence intensity is typically experienced at lower altitudes. Fig. 12 shows the results of the power spectrum and the line-of-best-fit for this case. Fig. 13 presents the identical case, but with 20 Hz wind data computed with the effects of wing flexure turned on. The slope of the line-of-best-fit, obtained via a least-squares analysis, for the case without wing flex considerations was −1.576, and the slope for the case with wing flex included was −1.614. It is clear that the refinements to the probe inertial velocity resulted in the slope of the power spectrum moving closer to the ideal value of −1.667. It is difficult to see obvious differences by simple inspection of these two cases. Wing flexure makes a relatively small, but positive contribution to the quality of turbulence calculations.

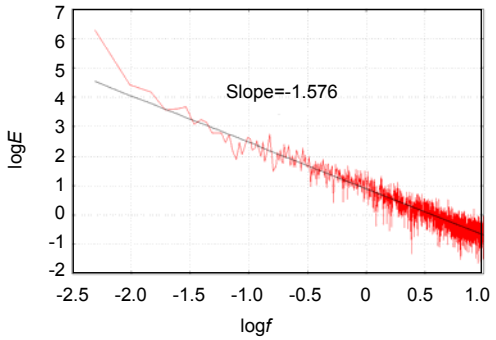

Fig. 12 Turbulence power spectrum without wing flexure velocity terms on Nov. 26, 2009

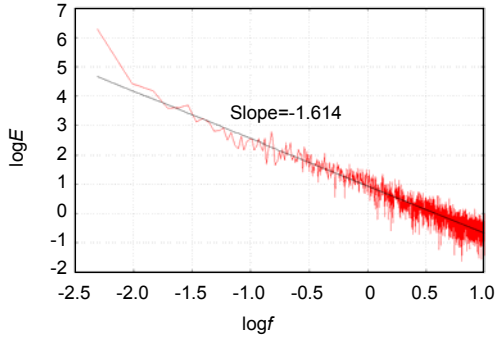

Fig. 13 Turbulence power spectrum including wing flexure velocity terms on Nov. 26, 2009

It is perhaps not too surprising that aero-elastic wing motion appears to have little effect on measured turbulence power spectra. Whatever the wing motion induced by unsteady aerodynamic forces, part of an oscillatory cycle could reduce the apparent vertical flow velocity only to cause the opposite to occur at a different part of the cycle. Upon reflection of these results, the most likely result of this process is to modify the phase of observed turbulent flow, not its energy content. This mechanism would have greater implications for airborne measurements that are very sensitive to flow signal phase, such as eddy correlation methods applied to turbulent flux calculations.

9 Impact of GPS-inertial improvements on wind data precision

As discussed in Section 2, the wind solution is a vector summation of the wind flow-velocity vector relative to the aircraft, transformed to a frame of reference parallel to the earth-fixed frame, plus the velocity of this aircraft frame relative to the earth. Precision of the wind solution will therefore depend directly on the repeatability of inertial velocity, orientation (Euler) angles, and air-data.

The extent to which inertial velocity precision has been improved was deduced by examining internal consistency between the complex IMU integration-Kalman filter process and the observed GPS velocity. If the system were perfect and error free, discrepancies between the IMU-filter system velocity output and the corresponding GPS observations would be zero. The amount of scatter in this measurement residual is a representation of the cumulative errors and uncertainties of the IMU-filter system. The behaviour of the inertial velocity residual relative to GPS is shown for the Nov. 26, 2009 calibration flight, indicating comparative results for the new algorithm formulation vs. the previous algorithm (Figs. 5–7). This exercise was repeated for the King's Park inter-comparison flight on Feb. 25, 2010, with the results illustrated by Figs. 14 and 15. RMS statistics were computed for the Feb. 25 case and the RMS residual for the north velocity from the previous algorithm was 0.051 m/s, and for the new algorithm was 0.021 m/s. For the east component, the corresponding values were 0.046 m/s and 0.022 m/s. This implies that precision of the horizontal inertial velocity components has been improved by about a few cm/s over the time period between filter updates (200 ms), due to improved IMU data handling between GPS refresh updates and better handling of the phase of GPS velocity updates.

The contribution to inertial velocity at the ADP

due to wing flexure was completely unaccounted for in the earlier processing-model formulation. The additional vertical velocity due to wing motion represents an instantaneous high-frequency vertical velocity error that has been removed (Fig. 16). The RMS magnitude of this velocity error from the flight of Feb. 25, 2010 was 0.25 m/s.

A similar argument can be made for attitude, using internal consistency improvements as an indicator of the degree of reduction in system noise and consequent improvement in measurement precision. As discussed in Section 2, the AIMMS-20 system utilizes two different Kalman filter designs to track attitude, one dependent on velocity matching (IMU vs. GPS), and the other dependent upon differencing the GPS carrier phase. Both algorithms resolve and track the same thing, namely, aircraft orientation. If both operated with zero error, then output from these two different approaches would be identical. Differences, therefore, reflect the degree of various uncertainties in the data, the system model and measurement model, and how they impact the different solution methods. Disagreement in the output sets a baseline for what we can expect in terms of precision. For example, if the two solutions can not agree to within 2°, then it is unlikely that we can be confident of either solution being significantly better than 2° in precision. Changes in consistency between the two different solution methods provide an indication of the extent of improvement to attitude precision.

True heading was chosen for this examination as heading most directly effects how the horizontal aircraft-relative flow vector is translated into wind-vector components in the earth-fixed reference frame. For example, at 100 m/s TAS, each degree in true heading error will result in a wind-component error of 1.75 m/s in the direction perpendicular to the flight track (by simple geometry). Reduction in heading noise is, therefore, very important to improving precision of the horizontal wind vector.

Fig. 17 illustrates the reduction in heading noise, for filter 2 (carrier-phase) output relative to filter 1 (IMU-GPS velocity matching). The original filter exhibits a RMS heading discrepancy over the complete flight of Feb. 25, 2010 of 0.13° and the new filter 0.08°. Although the improvement averaged over the entire flight is 0.05°, the previous algorithm suffered from periodic bursts where this discrepancy widened at times by a few tenths of a degree. Note that each 0.1° introduces a horizontal wind uncertainty of about 0.2 m/s at 100 m/s TAS.

Refined horizontal inertial velocity estimation and better stability for true heading have improved horizontal wind precision by 0.1 m/s on average and

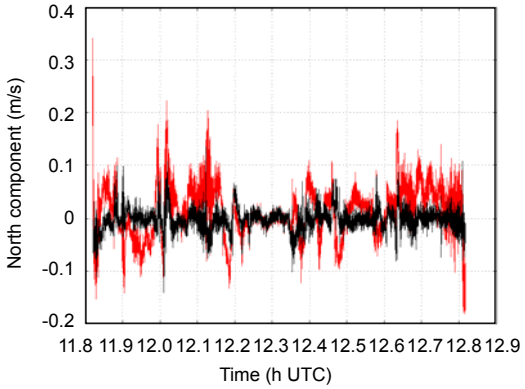

Fig. 14 North velocity residual before and after upgrades on the Feb. 25, 2010 Flight by GFS J4100
The red and black lines represent before and after algorithm upgrades, respectively (Note: for interpretation of the references to color in this figure legend, the reader is referred to the web version of this article)

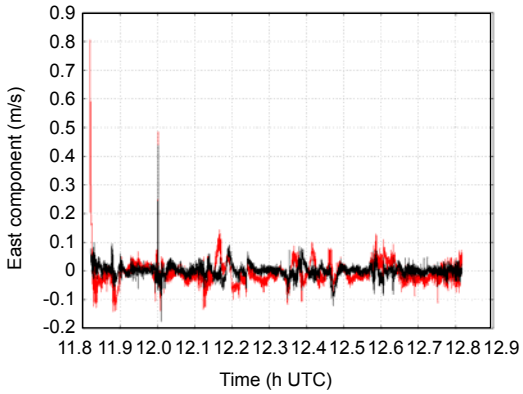

Fig. 15 East velocity residual before and after upgrades on the Feb. 25, 2010 Flight by GFS J4100
This figure used the same representations as in Fig. 14

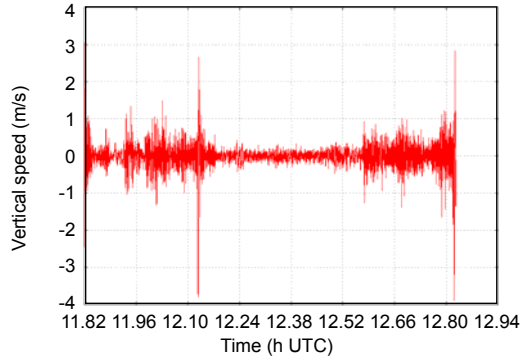

Fig. 16 Vertical wing-tip speed due to wring flexure on the Feb. 25, 2010 Flight by GFS J4100

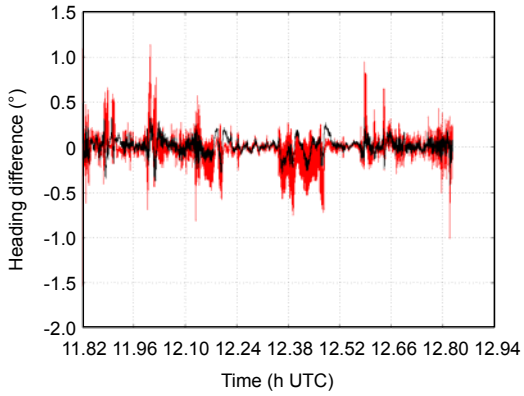

Fig. 17 True heading consistency of old algorithm vs. new algorithm on the Feb. 25, 2010 Flight by GFS J4100
The red and black lines represent before and after algorithm upgrades, respectively (Note: for interpretation of the references to color in this figure legend, the reader is referred to the web version of this article)

up to 0.2m/s or better during manoeuvres. Similarly, modelling wing flexure removed error in the instantaneous probe vertical velocity of about 0.25 m/s (RMS) under normal turbulence conditions typical of the mission of Feb. 25, 2010.

10 Validation of temperature lag correction

A simplified model for the influence of the enclosure on temperature response was developed in Section 6.1, and a method to evaluate the unknown parameters defining the response was discussed in Section 6.2. Parameter estimation according to the method discussed requires two things: (a) temperature output corresponding to a time-varying temperature environment; and (b) true atmospheric temperature as a function of time. Temperature output is obviously known, but the true-temperature input to the system is not easy to obtain with certainty. Even flying an ascent in parallel with a radiosonde launch introduces the question of spatial variability as the aircraft necessarily flies a slant-vertical profile whereas the balloon moves vertically.

The solution to this problem was to exploit the fact that the dynamic heating characteristic of the reverse flow housing geometry is known from independent wind-tunnel tests. Since airspeed is known very accurately, it is possible to predict changes in air temperature within the ventilation circuit that must result from airspeed changes with a high degree of confidence.

The altitude profile of the calibration flight of Nov. 26, 2009 is shown in Fig. 18 together with TAS. From about 8.6 h UTC to 9.15 h UTC flight altitude was maintained with excellent tolerance, mostly within ±25 m, during calibration manoeuvres.

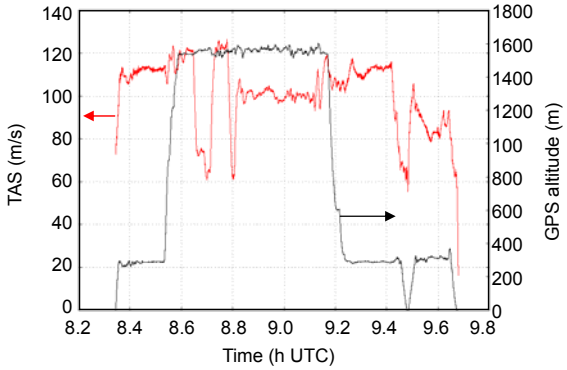

Fig. 18 Flight profile, airspeed and altitude on Nov. 26, 2009 by GFS J4100

The first calibration manoeuvre, which began by changing airspeed dramatically, started more than 3 min after the desired operating altitude was reached. This means that the thermal forcing due to altitude and airspeed changes was very small prior to the start of manoeuvres, sufficient to obtain a reading of temperature with most, if not all, lag effects extinguished. Knowing the lag-free temperature output at this altitude, and subtracting the dynamic heating contribution, we can obtain an excellent estimate for the "true" temperature T_0 at the calibration flight altitude. A narrow altitude band of ±25m meant that the atmospheric temperature should be stable to better than 0.25 °C, which is a limit based on the dry adiabatic lapse rate of 0.0098 °C/m. Therefore, after ignoring temperature variation due to altitude as being a small random error, we can obtain the following ideal temperature signal driven by TAS only (Nacass, 1992):

$$T(t)=T_0+\eta\frac{V^2(t)}{2C_{\mathrm{p}}}, \tag{78}$$

where η is the dynamic heating efficiency equal to 0.70 obtained by previous wind tunnel experiments, C_{p} is the mass-specific heat constant for dry air at a constant pressure (1004 J/(kg·K)), and $V(t)$ is the TAS as a function of time.

Eq. (78) becomes the basis for creating the set of ideal temperature values $\{T_i\}$ used to solve for unknown model parameters λ_{e} and α. Fig. 19 illustrates

the ideal temperature signal that was so constructed, driven purely by changes in TAS (black line), together with the actual measured temperature from the air-data probe (red line).

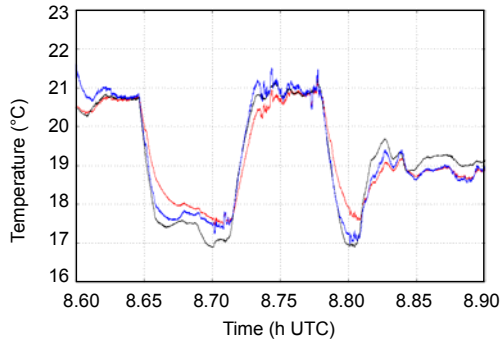

Fig. 19 Measured and ideal temperature with lag-corrected curve during speed variation at constant altitude on the Nov. 26, 2009 Flight by GFS J4100
The blue, black and red lines represent corrected, idea and measured temperatures, respectively (Note: for interpretation of the references to color in this figure legend, the reader is referred to the web version of this article)

The least-squares algorithm of Section 6.2 was applied using the ideal system temperature input and actual measured response output from the ADP thermistor. The least-square estimation resulted in the following optimum coefficient values: λ_e=0.0155 and α=0.369. The de-convolution described by Eq. (68) was then applied and the results are illustrated in Fig. 19 by the blue curve.

The value for λ_e may be interpreted as the reciprocal of the time constant for the housing material directly influencing ventilating flow temperature ($1/\lambda_e$ =65 s), and the value for α may be interpreted as representing about 1° output temperature bias for every 3° bias of housing temperature relative to the true temperature of the flow entering the ventilation tube.

Qualitatively, we can see behaviour of the lag correction scheme is reasonable. The lag-corrected and raw temperature curves come together during periods of slow temperature variation, and move furthest apart during periods of rapid change, with the measured data lagging behind.

The quality of the temperature lag-correction algorithm was verified using an independent dataset taken from a flight performed on Feb. 25, 2010 that included a slant-vertical profile flown at a time coordinated with the ascent of a radiosonde released from the King's Park Station in Hong Kong. The flight profile for the Feb. 25 flight is given in Fig. 20.

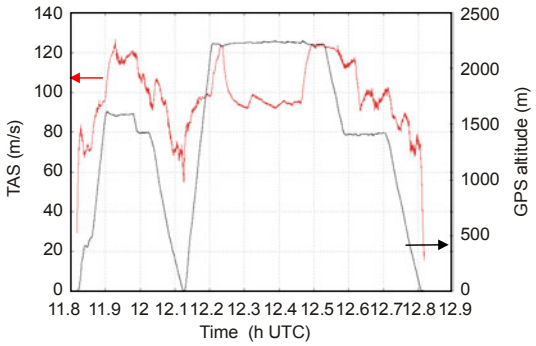

Fig. 20 Flight profile for King's Park radiosonde observation (RAOB) inter-comparison flight on Feb. 25, 2010 by GFS J4100

The slant-vertical profile was extracted from the processed dataset on the descent to the airport as this time matched most closely the time of release of the radiosonde (12 h UTC). The resulting temperature profile, both with the temperature as originally computed and the lag-corrected equivalent is shown together with the data from King's Park in Fig. 21.

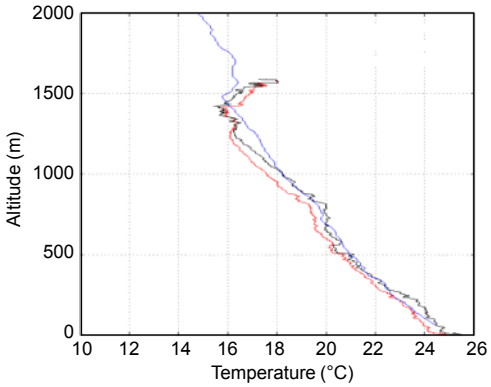

Fig. 21 Aircraft-radiosonde observation (RAOB) temperature inter-comparison on Feb. 25, 2010
The blue, black and red lines represent King's Park sounding temperature, lag-corrected and uncorrected temperatures, respectively (Note: for interpretation of the references to color in this figure legend, the reader is referred to the web version of this article)

The data was further analyzed to quantify bias as a function of altitude. Figs. 22 and 23 show the aircraft temperature profile data (red) and the 12 h UTC King's Park sounding (black) and the bias of the aircraft data (blue) with reference to the right-hand axis. Mean bias values were computed for both cases, in addition to the RMS scatter of the bias about the mean. Fig. 22 illustrates the case without lag correction, and Fig. 23 with lag correction turned on.

The values for mean bias and RMS deviation from the mean for the case without lag correction

were −0.34 and 0.53 °C, respectively. It is reasonable for the aircraft temperature to be lagging low as the aircraft profile at 12 h UTC was acquired on descent, i.e., the probe temperature was increasing as a function of time.

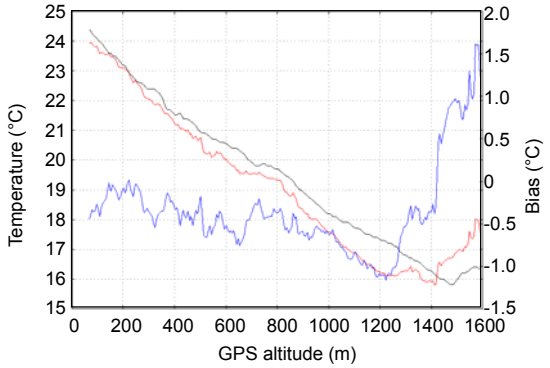

Fig. 22 Bias detail without lag correction on Feb. 25, 2010 by GFS J4100

The red, black and blue lines represent the aircraft temperature profile, the 12 h UTC King's Park sounding temperature and the bias of the aircraft data, respectively (Note: for interpretation of the references to color in this figure legend, the reader is referred to the web version of this article)

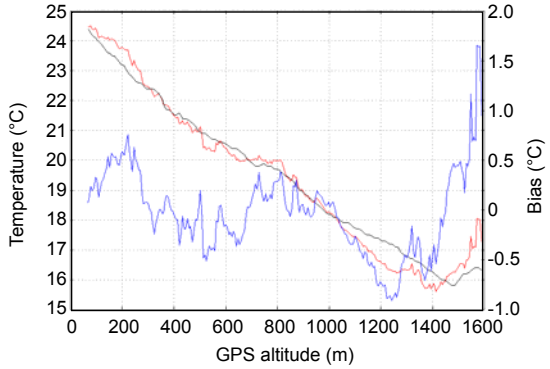

Fig. 23 Bias detail with lag correction on Feb. 25, 2010 by GFS J4100

This figure used the same representations as in Fig. 22

For the case with lag correction applied, the mean bias and RMS values were −0.02 and 0.43 °C, respectivley. Lag correction resulted in the aircraft temperature profile moving back and forth across the King's Park sounding resulting in a negligible mean offset. However, there was only a small improvement in the RMS bias deviation. The amount of scatter is likely due to factors other than aircraft-temperature frequency response, such as effects owing to real spatial and temporal variability of the atmosphere.

Additional inter-comparison cases were later acquired to further validate the qualities of the lag correction algorithm. Data were taken from flights performed on Apr. 30, 2012 and May 2, 2012 that included data from a slant-vertical profile data acquired at about the same time as an RAOB sounding from the nearby King's Park Station. Fig. 24 shows the temperature profile obtained in real time on descent to HKIA, with a touch-down time of 23.92 h UTC. The real-time data does not include any corrections for temperature lag induced by the sensor housing; but, the temperature profile obtained by the de-convolution algorithm implemented by the enhanced post-processing routine is included for comparison together with the King's Park 24Z RAOB sounding. The data clearly shows the cold bias of the descent profile, which is expected as the trajectory is taking the probe from cold conditions to progressively warmer conditions. The profile obtained from the de-convolved data, however, is moved significantly closer to the RAOB profile with a cold bias of from 1.0–1.5 °C reduced to less than 0.5 °C. The exercise was repeated on May 2 and the results showed similar behavior (Fig. 25). The profile after temperature de-convolution exhibited a cold bias on descent that is about 1/3 of the value obtained without correction.

11 Conclusions

In this paper, improvement of the accuracy of wind and temperature measurements of the AIMMS-20 system was achieved by applying a post-processing technique of the raw measurements. Wind measurements were improved by considering: (1) Error modelling of the accelerometer (e.g., bias offset and cross-axis rate sensitivity); (2) GPS phase lag (the finite time delay between the velocity update of the IMU and the GPS solution); (3) Better representation of the IMU velocity based on the GPS velocities considering their location difference; (4) Consideration of the slower (5 Hz) update of GPS velocity, i.e., taking angular acceleration into consideration during the 200 ms GPS data update; and (5) Wing flexure.

From the above considerations, the improvement in measurement of the horizontal wind would be in the order of 0.1 m/s on average and up to 0.2 m/s during manoeuvers. These figures represent an accuracy improvement of 20% over those originally specified in Section 1 (0.1/0.5 or 0.2/1).

Temperature measurements were improved by considering the temperature sensor response and the sensor housing response. From the above discussion,

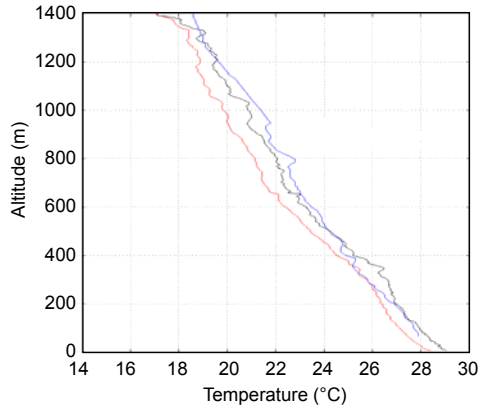

Fig. 24 Temperature descent profile to HKIA, 23.75–23.92 h UTC with lag-corrected profile and King's Park 24Z Sounding, Apr. 30, 2012

The blue, red and black lines represent the King's Park sounding temperature, temperature without and with deconvolution, respectively (Note: for interpretation of the references to color in this figure legend, the reader is referred to the web version of this article)

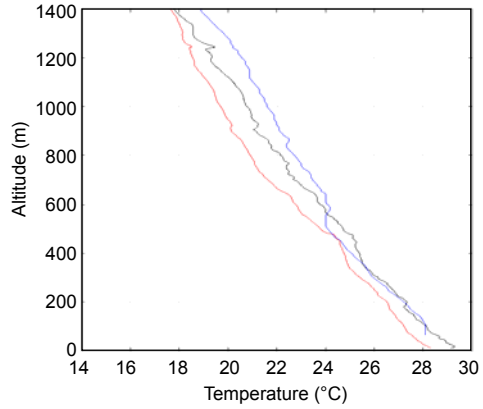

Fig. 25 Temperature descent profile to HKIA, 23.75–23.92 h UTC with lag-corrected profile and King's Park 24Z Sounding, May 2, 2012

This figure used the same representations as in Fig. 24

the bias of the temperature measurement was much reduced and the RMS error was reduced by about 0.1 °C by comparison with radiosonde data. This RMS error reduction is about 30% over the accuracy originally specified (0.1/0.3). For the remaining two meteorological measurements of AIMMS-20, namely, humidity and pressure, it is considered that post-processing of raw data is not expected to bring about significant improvement in their measurement.

The present paper discusses mainly the methodology for improving the accuracy of wind and temperature data from the AIMMS-20 with some examples for illustration purpose. The robustness of the methods so developed will be studied more systematically with a larger dataset, and the results will be presented in future papers.

References

Bögel, W., Baumann, R., 1991. Test and calibration of the DLR Falcon wind measuring system by maneuvers. *Journal of Atmospheric and Oceanic Technology*, **8**(1): 5-18. [doi:10.1175/1520-0426(1991)008<0005:TACOTD>2.0.CO;2]

Chan, P.W., Hon, K.K., Foster, S., 2011. Wind data collected by a fixed-wing aircraft in the vicinity of a tropical cyclone over the south china coastal waters. *Meteorologische Zeitschrift*, **20**(3):313-321. [doi:10.1127/0941-2948/2011/0505]

Dobosy, R.J., Crawford, T.L., MacPherson, J.I., Desjardins, R.L., Kelly, R.D., Oncley, S.P., Lenschow, D.H., 1997. Intercomparison among four flux aircraft at BOREAS in 1994. *Journal of Geophysical Research*, **102**(D24): 29101-29111. [doi:10.1029/97JD01174]

Drüe, C., Frey, W., Hoff, A., Hauf, T., 2008. Aircraft type-specific errors in AMDAR weather reports from commercial aircraft. *Quarterly Journal of the Royal Meteorological Society*, **134**(630):229-239. [doi:10.1002/qj.205]

Etkin, B., 1982. Dynamics of Flight: Stability and Control (2nd Edition). John Wiley & Sons, Inc.

Gelb, A., 1999. Applied Optimal Estimation. The MIT Press.

Inverarity, G.W., 2000. Correcting airborne temperature data for lags introduced by instruments with two-time-constant responses. *Journal of Atmospheric and Oceanic Technology*, **17**:176-184. [doi:10.1175/1520-0426(2000)017<0176:CATDFL>2.0.CO;2]

Khelif, D., Burns, S.P., Friehe, C.A., 1999. Improved wind measurements on research aircraft. *Journal of Atmospheric and Oceanic Technology*, **16**(7):860-875. [doi:10.1175/1520-0426(1999)016<0860:IWMORA>2.0.CO;2]

Lenschow, D.H., 1986. Probing the Atmospheric Boundary Layer. American Meteorological Society, Boston.

Matejka, T., Lewis, S.A., 1997. Improving research aircraft navigation by incorporating INS and GPS information in a variational solution. *Journal of Atmospheric and Oceanic Technology*, **14**(3):495-511. [doi:10.1175/1520-0426(1997)014<0495:IRANBI>2.0.CO;2]

Nacass, P.L., 1992. Theoretical Errors of Airborne Measurements of Static Pressure, Impact Temperature, Air-Flow Angle, Air-Flow Speed, TN-385. National Center for Atmospheric Research, Boulder CO, USA.

Rodi, A.R., Spyers-Duran, P.A., 1972. Analysis of time response of airborne temperature sensors. *Journal of Applied Meteorology*, **11**(3):554-556. [doi:10.1175/1520-0450(1972)011<0554:AOTROA>2.0.CO;2]

Rodrigues, E.A., Kamiyama, M.T., 1997. Computation of Dynamic Loads on Aircraft Structure due to Continuous Gust using MSC/NASTRAN. MacNeal-Schwendler Co.

Telford, J.W., Wagner, P.B., Vaziri, A., 1977. The measurement of air motion from aircraft. *Journal of Applied Meteorology*, **16**(2):156-166. [doi:10.1175/1520-0450(1977)016<0156:TMOAMF>2.0.CO;2]

Vörsmann, P., 1990. Meteopod, and airborne system for measurements of mean wind, turbulence, and other meteorological parameters. *Onde Electrique*, **70**:31-38.